Department of Physics and Astronomy

University of Heidelberg

Bachelor Thesis in Physics
submitted by

Maria Leticia Täubert

born in Stühlingen (Germany)

2017

Extreme ultraviolet spectroscopy of highly charged ruthenium ions

This Bachelor Thesis has been carried out by Maria Leticia Täubert
at the Max Planck Institute for Nuclear Physics in Heidelberg
under the supervision of
Priv.-Doz. Dr. José Ramón Crespo López-Urrutia

Abstract

Astronomical observations of elements heavier than iron in stars give insight into their stellar evolution. To understand the spectroscopic observations from such stars, atomic data of various trans-iron ions is required. Ruthenium ($Z = 44$) is of particular interest since its electronic structure is very similar to that of technetium ($Z = 43$), the lightest element with no stable isotopes. Due to the limited lifetime of technetium, its observation in stars provides a time scale of their evolutionary stages. In this thesis, ruthenium ions in the 8+ to 14+ charge states were investigated using an electron beam ion trap at the Max Planck Institute for Nuclear Physics in Heidelberg. Fluorescent light from excited ruthenium ions was recorded in the 17 – 27 nm wavelength range using a flat-field grazing incidence spectrometer. The spectra for Ru^{14+} and Ru^{15+} were analysed and compared with theoretical predictions. A total of 10 electronic transitions were identified. These constitute the first set of experimental data with sufficient precision for astrophysical models.

Zusammenfassung

Astronomische Beobachtungen von Elementen schwerer als Eisen in Sternen geben einen Einblick in ihre stellaren Evolution. Um die spektroskopischen Beobachtungen von solchen Sternen zu verstehen, sind Atomdaten verschiedener Trans-Eisen-Ionen erforderlich. Ruthenium (Z=44) ist von besonderem Interesse, da seine elektronische Struktur der von Technetium sehr ähnlich ist (Z=43). Technetium ist das leichteste Element ohne stabile Isotope. Wegen der begrenzten Lebensdauer von Technetium bietet seine Beobachtung in Sternen eine Zeitskala ihrer evolutionären Stufen. In dieser Arbeit wurden Rutheniumionen in den 8+ bis 14+ Ladezuständen unter Verwendung einer Elektronenstrahl-Ionenfalle am Max-Planck-Institut für Kernphysik in Heidelberg untersucht. Fluoreszenzlicht aus angeregten Rutheniumionen wurde im Wellenlängenbereich von 17 – 27 nm unter Verwendung eines Flachfeld-Weide-Inzidenzspektrometers aufgezeichnet. Die Spektren für Ru^{14+} und Ru^{15+} wurden analysiert und mit theoretischen Vorhersagen verglichen. Es wurden insgesamt 10 elektronische Übergänge identifiziert. Diese stellen den ersten Satz von experimentellen Daten mit hinreichender Genauigkeit für astrophysikalische Modelle dar.

Contents

1 Motivation

Ever since the first observation of dark features in the solar spectrum by Fraunhofer in the early 19$^{\text{th}}$ century, spectroscopy has played a major role in the development of modern physics. Fraunhofer's observation led Kirchhoff and Bunsen to discover the link between absorption and emission lines, namely that the solar spectral lines coincide with the emission lines of several chemical elements, thereby concluding that the lines were caused by light absorption by elements in the sun's atmosphere [1]. In the late 19$^{\text{th}}$ century, J. Balmer discovered that the discrete lines in the visible spectrum of hydrogen could be described by an integer series, which eventually led to the Rydberg formula and the development of the Bohr model of the atom. The Bohr model describes the atom as consisting of a point-like, positively charged nucleus that is orbited by negatively charged electrons. This model, though intrinsically incorrect, continues to be useful today as an introduction to atomic structure. With improving technology, spectral measurement devices could increasingly be used for astronomical observations. Indeed, Fraunhofer's discovery was only possible due to the development of the first modern spectrometer.

The first star to be extensively studied was the Sun. It is commonly called a yellow-dwarf star, and it produces a large amount of radiation, including in the ultraviolet wavelength regime. Since earth's atmosphere is opaque to the UV radiation from space, a number of satellites missions were planned to observe the Sun, e. g., *Solar Dynamic Observatory (SDO), Solar-C, Hinode, SOHO*, and sounding rockets [3]. By observing UV radiation from the Sun, not only the elemental abundance, but also the electron density and temperature could be estimated, which is very critical to understand the inner workings of the Sun. One of the observed spectra from SDO in the ultraviolet wavelength regime is given in figure 1.1. The figure

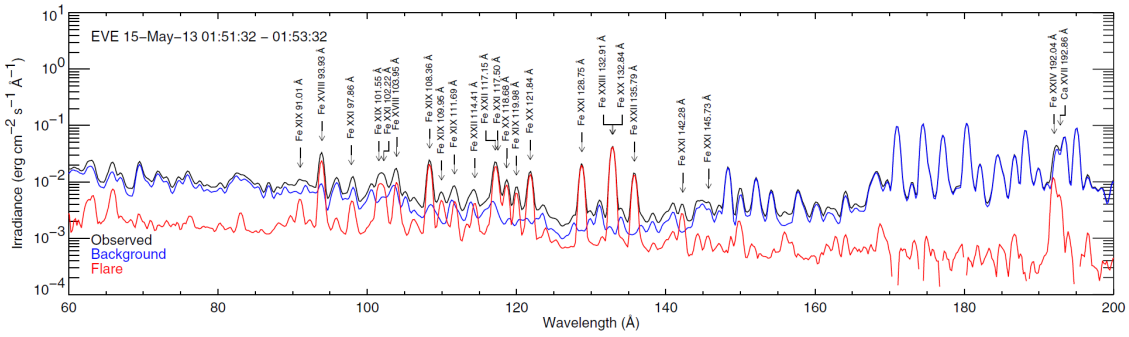

Figure 1.1: Observation of solar flares in the EUV region. Emission lines from the Fe XVIII to Fe XXIV spectrum are identified [2].

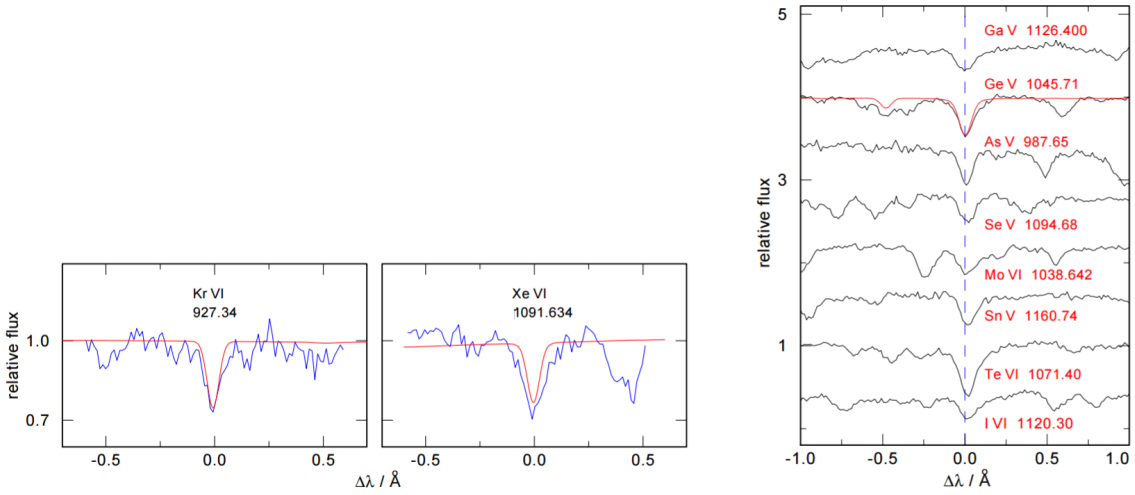

Figure 1.2: Left: Observed krypton and xenon lines for the charge state VI (blue) and the model from Werner *et al.* (red). Right: Lines from eight trans-iron group elements observed in the white dwarf star RE 0503-289 [4].

shows various ions, e.g, Fe and Ca, ejected during the the Solar flare including various electronically excited transitions. For this reason, analysing spectral data from stars is highly important for astronomers: it is a key resource for the study of stellar evolution and composition. Various astrophysical models are used to achieve this, but to be able to comprehensively analyse these spectra, having spectral atomic data is vital.

One particular star that has been of interest in recent years is the white dwarf RE 0503 289. It was first observed in 1994 by Barstow *et al.* [5], and shortly after it was determined that it is a hot helium-rich white dwarf [6]. This was surprising, since most white dwarfs are hydrogen-rich, and it raised questions about the evolutionary history of helium-rich stars.

One prevailing theory is that a late helium-shell flash in preceding evolutionary stages is the cause of the hydrogen deficiency. A helium-shell flash is a brief thermal runaway nuclear fusion reaction of helium that causes mixing and burning of surface hydrogen, dredging up material from deep layers to the surface. It's expected that this would cause trans-iron elements (which were created by nucleosynthesis processes when the star was in the "asymptotic giant branch (AGB)" phase) to be found in large abundance in the star surface. The exact abundances would then give clues to the type of nucleosynthesis processes that were occurring during the ABG phase, bringing more clarity to the evolutionary history of the helium-rich white dwarf RE 0503 289.

In 2012, Werner *et al* identified an over abundance of xenon, krypton and other trans-iron elements in RE 0503 289 [4] (see figure 1.2). They were found in quantities in the range between 155 and 23 000 times solar, which are much larger than what is found in hydrogen-rich stars. This seems to indicate that a late helium-shell flash occurred. However, more proof is needed to be certain of the evolutionary history

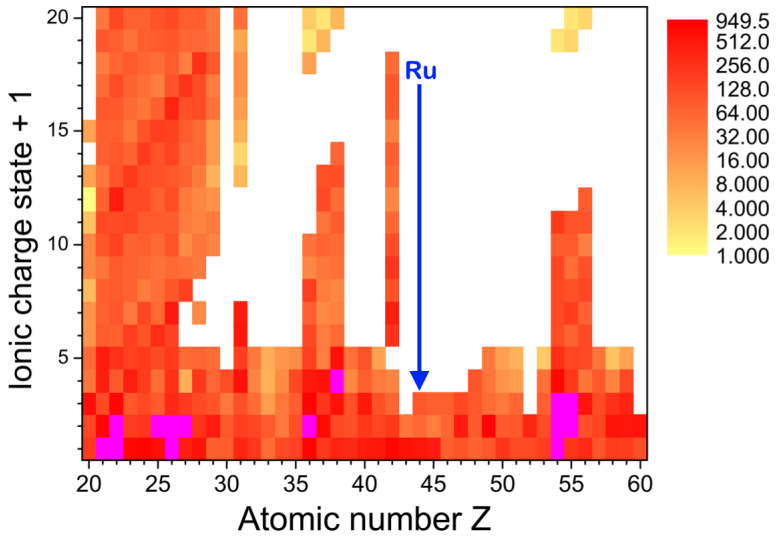

Figure 1.3: Ionic charge state plotted against the atomic number Z. The coloured rectangles mark the amount of known lines the species has. Charged states for which no reported atomic data is known are marked in white. Technetium and ruthenium have no known data beyond Tc II and Ru III (from [8]).

of the star. Observing technetium (Z=43) is what would be decisive, because it is the first element with no stable isotopes and "its presence would be convincing proof that the high trans-iron abundances are directly related to the occurrence of a late helium shell flash in preceding evolutionary stages" [7].

The main impediment for the identification of Tc in the stellar data is the lack of atomic data available. This is clearly seen in figure 1.3, which showcases the "sea of ignorance", where ions with no reported experimental data whatsoever are marked in white. It can be seen that all the atomic data for technetium after Tc II is unknown. Measuring Tc in the laboratory is currently a challenge, since to work with radioactive material extensive changes need to be made to the measurement devices presently available. It was thus decided to measure ruthenium first, since it's not radioactive and it also lacks a high number of experimental data. Ruthenium has the atomic number 44 and lies beside technetium in the periodic table. It therefore has a very similar electronic structure to Tc, which makes it viable to study.

Measurements in the extreme ultraviolet regime from heavy ions like ruthenium are also critical to study electron-electron interactions and to benchmark theoretical atomic physics. This is because the basic approach of describing the repulsive interactions between the electrons as product of uncorrelated single-particle wave functions isn't accurate after the hydrogen atom. The wavefunction increases in complexity the more electrons are involved, which makes it challenging to compute level energies and line positions with a high level of accuracy. Measurements of many electron systems like ruthenium are therefore increasingly used to test model calculations [9, 10].

Our goal is to observe ruthenium transitions in the ultraviolet range and identify

their charged state. Electron Beam Ion Traps (EBIT) are a great tool to study such spectra. They allow the creation, trapping and spectral analysis of highly charged ions (HCI). EBITs can go through a wide range of energies, meaning that the spectral selectivity afforded by EBITs can be very high, since every time the energy surpasses the ionization potential of a given species, the next higher charge state is produced. This, along with the EUV spectrometer used to record the spectra, easily permits the study of ruthenium ions.

Outline of the thesis

In this thesis, we study and identify ruthenium ions in the extreme ultraviolet range. We present the experimental method that was used and showcase the measurement results.Having such data serves astronomical and theoretical purposes. This thesis is structured in the following way.

- In Chapter 2 we review the basics of quantum mechanics and the rules for electronic transitions. We also discuss the various atomic processes that take place in an EBIT.
- In Chapter 3 we describe the experimental setup used to take EUV spectra of Ru-ions. We describe the main components of the FLASH-EBIT and the EUV spectrometer.
- In Chapter 4 we discuss the recording of the Ru-ion spectra, corrections that need to be made to the measured data, the calibration process and the preliminary identification of different charge states.
- Chapter 5 focuses on the identification of Ru^{14+} and Ru^{15+} and the comparison to theoretical calculations.
- Chapter 6 summarises the results presented in this thesis, and gives an outlook to future measurements and analysis.

2 Theoretical background

This chapter introduces basic concepts in quantum mechanics and atomic physics, starting with the hydrogen atom and its solution, moving on to the selection rules for transitions from one quantum state to another and discussing the atomic processes that take place in an electron beam ion trap (EBIT).

2.1 Hydrogen atom

The hydrogen atom consists of one electron and proton. As a one-electron system, it has a very simple electronic configuration. The wave function $\Psi(t)$ describes this system. To find $\Psi(t)$ we must first solve the Schrödinger equation:

$$H\Psi(t) = E\Psi(t), \tag{2.1}$$

where H represents the Hamiltonian and E the energy.

The Hamilton operator is the sum of operators corresponding to the kinetic and potential energies of the system. In the case of hydrogen-like atoms (with a nucleus N and an electron e), the following equation holds:

$$H = -\frac{P_{\mathrm{N}}^2}{2m_{\mathrm{N}}} - \frac{P_{\mathrm{e}}^2}{2m_{\mathrm{e}}} - \frac{Ze^2}{4\pi\epsilon_0|\vec{r_{\mathrm{N}}} - \vec{r_{\mathrm{e}}}|}, \tag{2.2}$$

where P is the momentum operator, m is the mass, Z represents the number of protons in the nucleus, e is the charge of the electron, ϵ_0 the electric permeability, and $\vec{r}$ is the position vector.

In order to solve the Schrödinger equation we introduce relative (rel) and centre of mass (com) coordinates:

$$H = -\frac{P_{\mathrm{com}}^2}{2M} - \frac{P_{\mathrm{rel}}^2}{2\mu} - \frac{Ze^2}{4\pi\varepsilon_0 r} = H_{\mathrm{com}} + H_{\mathrm{rel}}, \tag{2.3}$$

where μ is the reduced mass $\left(\frac{m_{\mathrm{e}} \cdot m_{\mathrm{N}}}{m_{\mathrm{e}} + m_{\mathrm{N}}}\right)$, M the total mass, and r the distance between the nucleus and the electron.

Since equation (2.3) is separable, it can be solved via a product ansatz: $\Psi = \psi_{\mathrm{com}} \cdot \psi_{\mathrm{rel}}$. It is more interesting to find the eigenstates of H_{rel}, as the eigenstates of H_{com} are free-particle eigenstates, and are hence trivial. The relative Hamiltonian can be solved by using the position-space representation of the momentum operator:

$$\left[-\frac{\hbar^2\vec{\nabla}^2}{2\mu}-\frac{Ze^2}{4\pi\varepsilon_0 r}\right]\psi(\vec{r})_{\mathrm{rel}}=E_{\mathrm{rel}}\psi(\vec{r})_{\mathrm{rel}}, \tag{2.4}$$

where $\hbar$ is the reduced Planck constant, $\vec{\nabla}$ is the Laplacian, $\vec{r}$ is the relative position vector, E_{rel} is the eigen energy of the relative Hamiltonian, and $\psi(\vec{r})_{\mathrm{rel}}$ is the wavefunction of the relative Hamiltonian.

We have spherical symmetry in equation (2.4), so therefore we expand the Laplacian in spherical coordinates and use the separation ansatz $\psi(\vec{r})_{\mathrm{rel}}=R(r)Y(\vartheta,\varphi)$:

$$\left\{-\frac{\hbar^2}{2\mu r^2}\left[-\frac{\partial}{\partial r}\left(r^2\frac{\partial}{\partial r}\right)-\frac{\vec{L}^2(\vartheta,\varphi)}{\hbar^2}\right]-\frac{Ze^2}{4\pi\varepsilon_0 r}\right\}R(r)Y(\vartheta,\varphi)=E_{\mathrm{rel}}R(r)Y(\vartheta,\varphi), \tag{2.5}$$

where $\vec{L}(\vartheta,\varphi)$ is the angular momentum in spherical coordinates (with the eigenstates $l(l+1)\hbar^2$), $R(r)$ is the radial part and $Y(\vartheta,\varphi)$ are spherical harmonics.

Finally, this expression is separated and the radial part is rearranged to give the final solution:

$$-\frac{\hbar^2}{2\mu}\frac{\partial}{\partial r^2}U(r)+\left[\frac{\hbar}{2\mu r^2}l(l+1)-\frac{Ze^2}{4\pi\varepsilon_0 r}\right]U(r)=E_{\mathrm{rel}}U(r), \tag{2.6}$$

where $U(r)=r\cdot R(r)$.

In equation 2.6 we have essentially reduced the Schrödinger equation for the hydrogen atom to an effective one dimensional problem that only depends on the radial distance. The eigenenergy can be calculated and it turns out to be:

$$E_{\mathrm{n}}=-\frac{Z^2\cdot 13.6\mathrm{eV}}{n^2}, \tag{2.7}$$

where $n\in\mathbb{N}\setminus\{0\}$ is the principal quantum number.

More details can be found in the book "Physics of Atoms and Molecules" [11] and in the lecture notes of S. Jochim [12], as well as most books relating to the basics of quantum mechanics.

2.2 Selection rules

Selection rules lay out the possible transitions from one quantum state to another when interacting with the electromagnetic field i.e. light.

In the case of an electric dipole interacting with light there are a few steps one needs to take in order to derive these rules. We assume that the classical electric

field of light $\vec{E}$ interacts with the atom and that $\vec{E}$ is constant at the centre of mass position of the atom. Then we model the atom as a two state system, with a ground state $|1\rangle$ and an excited state $|2\rangle$.

The transition probability of $|1\rangle \rightarrow |2\rangle$ is:

$$P_{1\rightarrow 2} = -\frac{E_0^2}{2\hbar^2} |\langle 2|\vec{D}\vec{\epsilon}|1\rangle|^2 \frac{\left(\sin\frac{\Delta t}{2}\right)^2}{\left(\frac{\Delta t}{2}\right)^2}, \tag{2.8}$$

where $\vec{E}_0$ is the , $\vec{D}$ is the dipole moment, $\vec{\epsilon}$ is the polarisation vector, t is the time, and $\Delta = (\omega - \omega_0)$, with ω_0 being the frequency of the light and ω the transition frequency.

The matrix element $\langle 2|\vec{D}\vec{\epsilon}|1\rangle$ can be expressed in terms of the electronic configuration, and the total angular momentum and its projection. If we separate the dipole matrix element in spherical components, then we reach an expression composed of the reduced matrix element and the so called Clebsh Gordan-Coefficients.

The selection rules are then derived from the Clebsh Gordan-Coefficients, since the transition probability is zero when they vanish. For the electric dipole, the coefficients don't vanish in the case that:

$$\begin{aligned} &\text{(I)} \quad \Delta J = 0, \pm 1, \\ &\text{(II)} \quad \Delta M_J = 0, \pm 1, \\ &\text{(III)} \quad \text{The parity changes i.e } \pi_f = -\pi_i, \end{aligned} \tag{2.9}$$

where J is the total angular momentum, M_J is the projection of the total angular momentum, and the parity is a flip in the sign of the spatial coordinate, so the initial parity π_i changes to the final parity $-\pi_f$. This means that the parity changes.

The rules are derived in this manner from the Clebsch Gordan-Coefficients. A short summary of the rigorous selection rules is given in table 2.1.

Table 2.1: Selection rules for the E1, M2 and E2 transitions [13].

	Electric dipole (E1)	Electric dipole (M1)	Electric quadrupole (E2)
(1)	$\Delta J = 0, \pm 1$ (No $J = 0 \leftrightarrow 0$)	$\Delta J = 0, \pm 1$ (No $J = 0 \leftrightarrow 0$)	$\Delta J = 0, \pm 1, \pm 2$ (No $J = 0 \leftrightarrow 0, 1; \frac{1}{2} \leftrightarrow \frac{1}{2}$)
(2)	$\Delta M_J = 0, \pm 1$	$\Delta M_J = 0, \pm 1$	$\Delta M_J = 0, \pm 1, \pm 2$
(3)	Parity change	No parity change	No parity change

2.3 Atomic processes taking place in an EBIT

There are several processes by which electron-ion interaction can take place, including bremsstrahlung, radiative recombination, electron impact ionization, photoionization, electron impact excitation/de-excitation, dielectronic recombination and higher-order recombination processes.

- The most common process is Bremsstrahlung, in which an electron is decelerated by being deflected in the electric field of an ion:

$$\mathrm{A}^{\mathrm{q}+} + \mathrm{e}^{-}(E_{\mathrm{i}}) \rightarrow \mathrm{A}^{\mathrm{q}+} + \mathrm{e}^{-}(E_{\mathrm{f}}) + \gamma, \tag{2.10}$$

  where E_{i} and E_{f} represent the initial and final kinetic energy of the electron.

- Radiative recombination is the time-reverse process of photoionization. A free electron is captured into the ion, and a photon of energy $\hbar\omega$ is emitted ($\hbar\omega$ is the sum of the kinetic energy of the free electron and the binding energy of the bound electron):

$$\mathrm{A}^{\mathrm{q}+} + \mathrm{e}^{-} \rightarrow \mathrm{A}^{(\mathrm{q}-1)+} + \gamma. \tag{2.11}$$

- Electron impact ionization occurs when a free electron collides with a bound electron, on the condition that the kinetic energy of the free electron surpasses the ionization potential of the bound electron:

$$\mathrm{A}^{\mathrm{q}+} + \mathrm{e}^{-} \rightarrow \mathrm{A}^{(\mathrm{q}+1)+} + 2\mathrm{e}^{-}, \tag{2.12}$$

  where q refers to the charge state of the ion A, and e to the electron.

- Photoionization occurs when the bound electron interacts with a photon γ with an energy higher than the binding energy of the electron:

$$\mathrm{A}^{\mathrm{q}+} + \gamma \rightarrow \mathrm{A}^{(\mathrm{q}+1)+} + \mathrm{e}^{-}. \tag{2.13}$$

  Photons in the UV and X-ray range are needed in order for photon absorption ionization to occur in highly charged ions [14].

- Electron impact excitation/de-excitation is a process by which an electron is brought to an energetically higher state after a collision with a free electron, and is later de-excited after a certain amount of time, thereby releasing a photon γ in the process:

$$\mathrm{A}^{\mathrm{q}+} + \mathrm{e}^{-} \rightarrow \mathrm{A}^{\mathrm{q}+*} + \mathrm{e}^{-} \tag{2.14}$$

$$\mathrm{A}^{\mathrm{q}+*} + \mathrm{e}^{-} \rightarrow \gamma + \mathrm{A}^{\mathrm{q}+} + \mathrm{e}^{-}. \tag{2.15}$$

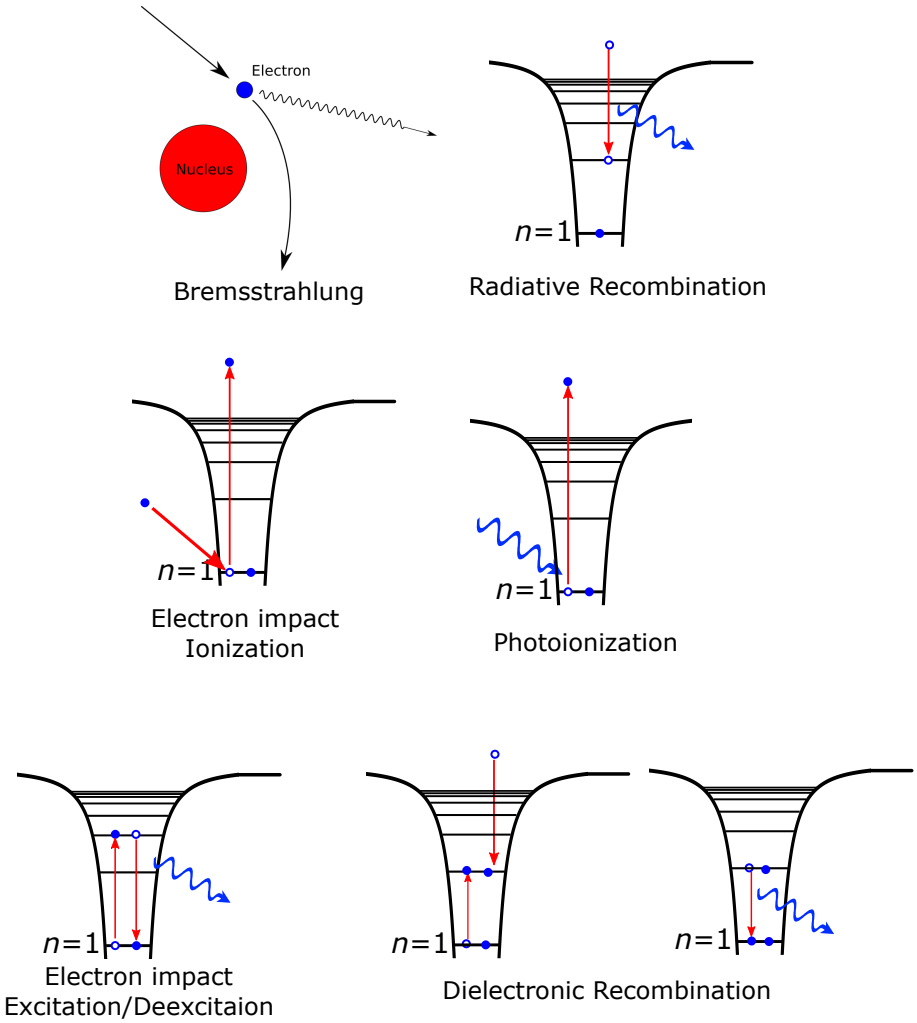

Figure 2.1: Visual representation of the atomic processes taking place in an EBIT. Radiative recombination, electron impact ionization, photoionization and dielectronic recombination involve a change in the final charge state of the ion. Bremsstrahlung results in the deflection of a free electron. Electron impact excitation/de-excitation involves the release of a photon after a bound electron is brought to a higher state and is later de-excited.

Electron impact excitation can occur only when the kinetic energy of the electron E_e is greater than or equal to the energy difference between the initial and final states:

$$E_e \geq E_f - E_i \tag{2.16}$$

This condition are easily met in an EBIT, since the electron beam energy E_{beam} can be modified over a wide range of energies. Hence, electron impact excitation is continuously taking place, generating the observed fluorescence. Since the free electron transfers kinetic energy to the bound electron, which is then stored as potential energy, it is possible to attain any excited level independently of selection rules. The electrons then continuously cascade down to the ground state, thereby generating radiation. This means that potentially the full spectrum can be observed when doing spectral measurements [15].

- Dielectronic recombination (DR) is a resonant process by which a free electron is captured into an ion, promoting a bound electron from a lower to a higher shell. This intermediate excited state is unstable and it radiatively decays to the ground state. A photon characteristic to the excited state is then emitted:

$$A^{q+} + e^- \rightarrow [A^{(q-1)+}]^{**} \rightarrow A^{(q+1)+} + \gamma. \tag{2.17}$$

Since dielectronic recombination is a resonant process, it can only take place if the following condition is met [16]:

$$E_e + E_b = \Delta E_{core}, \tag{2.18}$$

where E_b represents the binding energy of the recombined state, and ΔE_{core} the difference between the core electron state and the state in which the second electron is excited.

The notation to describe DR is the following: First the shell of the ground state is named, then the shell of the promoted electron, and lastly the shell into which the free electron in captured. So if an electron is captured into the L shell, and it promotes an electron from the K to the L shell, that DR process would be called KLL. Other processes such as KLM, KLN, LLM, LMN, etc could also take place depending on the energy of the free electron and the ionization level of the ion.

3 Experimental setup

3.1 Electron beam ion trap

The electron beam ion trap (EBIT) is one of the best available techniques to create, trap and study highly charged ions. Since all the measurements discussed in this thesis were realized at the FLASH-EBIT in the Max Planck Institute of Nuclear Physics in Heidelberg, I will go into further detail about this specific EBIT.

Every EBIT consists of three main parts: The electron gun, the magnet chamber and the collector (see figure 3.1) The electron gun emits the electrons, the magnet chamber focuses them into a beam, thereby creating the ion trap, and the collector captures the electron beam. The ions are trapped radially by the beam's space charge potential and axially by the electrostatic potential of the drift tubes. The atoms to be studied are introduced into the EBIT via the injection system.

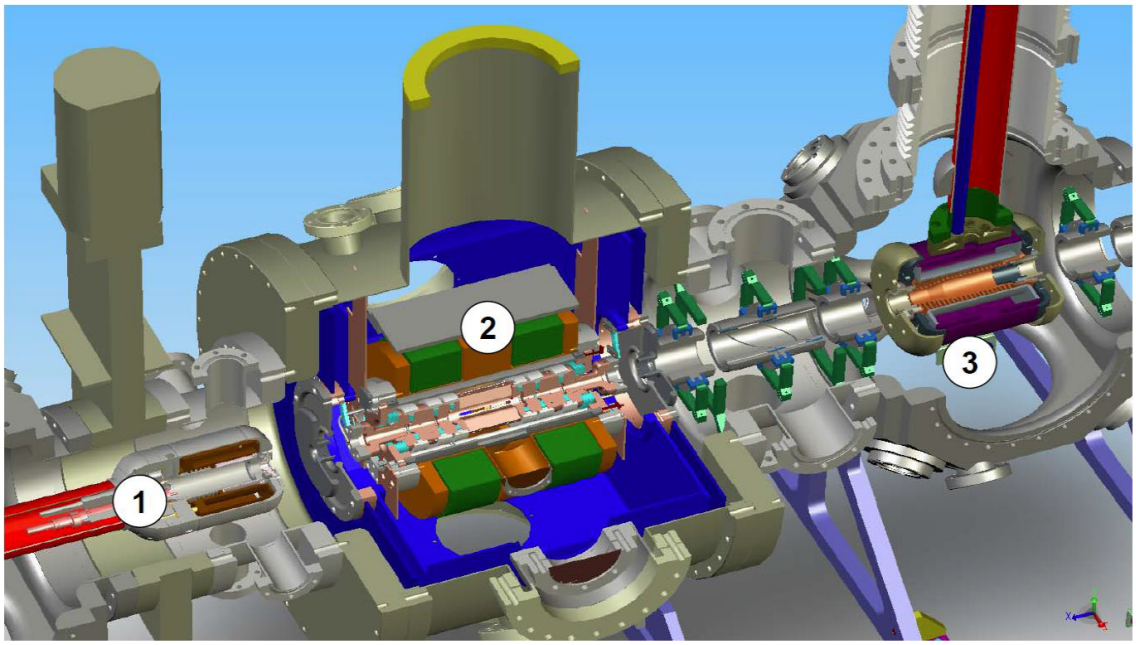

Figure 3.1: Cross-sectional view of the FLASH-EBIT: (1) electron gun consisting of a cathode that emits electrons accelerated towards the anode, (2) magnet chamber consisting of 9 drift tubes and superconducting Helmholtz coils, (3) collector consisting of various electrodes, the suppressor and the extractor, which are surrounded by the front and back shields respectively (from [16]).

3.1.1 The electron gun

The goal of the electron gun is to generate electrons that are then focused into a beam by the surrounding electric field. The electron gun consists of a cathode made of a tungsten heating filament coated with barium oxide, an anode with the shape of a hollow cylinder and a focus-electrode that serve to pull away the electrons from the surface of the cathode. The cathode is heated to about 1300−1500 K and emits electrons through thermo-ionic emission. The voltage in the cathode is typically around −2 kV. The potential difference between the cathode and the anode causes an acceleration of 2 kV.

A residual magnetic field from the ion trap can reach the electron gun. This can cause the beam radius to increase, thereby lowering the ionisation rate [16]. To counteract this rest field, trimming and bucking coils are placed around the cathode.

The electron gun can be moved along the vertical and horizontal axis perpendicular to the beam, as well as parallel to the beam direction. This means that the electron gun can be completely removed from the rest of the EBIT and into its own vacuum chamber, allowing for the gun to be kept at very low pressures ($< 10^{-10}$ mbar) while the Magnet chamber is under atmospheric pressure, which is required to attach a new detector [17].

3.1.2 Electron beam properties

The electron beam radius, an important property of the EBIT, was first calculated by L. Brillouin in 1945 [18], who assumed that all the electrons are travelling in the same direction without intersecting each others trajectories (laminar flow) and that the electrons are produced in a region with zero magnetic field, as well as not taking into account the initial thermal energy of the electrons. The electron beam radius r_B calculated by Brillouin was:

$$r_\mathrm{B} = \sqrt{\frac{2m_\mathrm{e}I_\mathrm{beam}}{\pi\varepsilon_0 v_\mathrm{e} e B^2}}, \tag{3.1}$$

where m_e is the electron mass, e is the electron charge, I_beam is the electron beam current, ε_0 is the permittivity of vacuum, v_e is the electron speed and B is the axial magnetic field.

Brillouin's theorem was then expanded on by G. Hermann, who took into account the contributions arising from the cathode. Under the assumption that the axial velocity of the electrons is independent of the radial position, the beam radius r_beam constitutes of the radius r_B multiplied by a factor coming from the initial thermal energy of the electron and the magnetic field used for compression [19]:

$$r_\mathrm{beam} = r_\mathrm{B}\sqrt{\frac{1}{2}+\frac{1}{2}\sqrt{1+4\left(\frac{8m_\mathrm{e}k_B T_c r_c^2}{e^2 r_\mathrm{B}^2 B^2}+\frac{B_c^2 r_c^4}{B^2 r_\mathrm{B}^2}\right)}}, \tag{3.2}$$

where k_B is the Boltzmann constant and T_c , r_c and B_c are the temperature, radius and surface magnetic field strength of the cathode, respectively.

The total potential difference $E_{\text{beam}}$of the electron beam can be calculated:

$$E_{\text{beam}} \approx |V_{\text{cathode}}| + |V_{\text{platform}}| + |V_{\text{trap}}| - |V_{\text{beam sp}}|, \tag{3.3}$$

where V_{cathode} is the potential in the cathode, V_{platform} is the potential added to the drift tubes, V_{trap} is the voltage of the central drift tube, and $V_{\text{beam sp}}$ is the space charge potential created by the electron beam itself.

The space charge potential $V_{\text{electron sp}}$ coming from the electrons can be approximated by the following equation [20]:

$$V_{\text{electron sp}}[\text{V}] \approx \frac{30 I_{\text{beam}}[\text{A}]}{\sqrt{1 - \left(\frac{E_{\text{e}}[\text{keV}]}{511} + 1\right)^{-2}}} \left(\ln \left(\frac{r_{\text{beam}}}{r_{\text{dt}}} \right)^2 - 1 \right), \tag{3.4}$$

where E_{e} is the electron energy , r_{dt} the radius of the drift tubes and r_{beam} the radius of the electron beam.

In the framework of this thesis, the electron beam space charge was estimated using equation (3.4). But this negative space charge arising from the atoms had to in turn be corrected for the positive space charge coming from the ion cloud. This can account for negligible to close to 100 % compensation of the electron space charge potential, mostly depending on the depth of the trap: a shallow axial trap causes less compensation, since axial ion escape dominates, and a deep trap can cause complete compensation, since radial escape dominates [21]. Therefore the following equation has to be used to estimate the total beam energy:

$$E_{\text{beam}} \approx |V_{\text{cathode}}| + |V_{\text{platform}}| + |V_{\text{trap}}| - |V_{\text{electron sp}}| + |V_{\text{ion sp}}|, \tag{3.5}$$

where $|V_{\text{ion sp}}|$ is the space charge contribution from the ion cloud.

3.1.3 The ion trap

The ion trap consists of nine ring shaped drift tubes surrounded by superconducting Helmholtz coils that trap the electrons into a very thin beam of below 50 μm. The superconducting magnet, composed of Nb_3S, is made by the company Cryogenics. It achieves a magnetic field strength of 6 T with a current of 114 A. It is to note that the configuration of the Helmholtz coils was chosen to allow for better radial access to the trap, as opposed to creating the most homogeneous magnetic field: there are 7 holes drilled into the magnet chamber, which are all perpendicular to the electron beam. They consist of two horizontal holes, one vertical hole and four holes at a 45 °angle to the horizontal holes [17].

The nine drift tube electrodes can collectively reach a voltage of 30 kV. This makes it possible to vary the electron beam energy over a large range of energies. The central drift tube contains 8 slits (7 of which can be accessed via the holes in the magnet) that allow a view into the centre of the trap so that various detectors can be attached. This permits simultaneous measurements in different wavelength regimes with more than one photon detector. Additional electrodes are found between the drift tubes and the collector to facilitate the refocussing of the electron beam or ion cloud in the case of an extraction.

The ions are radially trapped by the negative space charge of the electron beam, and axially trapped by the voltages applied to the drift tubes. Since the drift tube voltages can be changed, it is possible to set the trap to be shallow or deep. A shallow trap is used when evaporative cooling is required, and a deep trap is chosen the the ion temperature is less important [22]. A schematic diagram of the trap region is shown in figure 3.2.

3.1.4 The collector

The collector is used to capture the electron beam. It consists various electrodes, the front and back shields, and the suppressor and the extractor, that guide the beam, and a magnetic coil that minimizes the rest magnetic field from the trap region and thus expands the beam. The magnetic coil and the inner part of the collector are cooled using water. The extractor has a more negative potential compared to the cathode, meaning that the electrons which now have a maximum kinetic energy of 2keV can be slowed down and guided to the inner side of the collector. The collector is insulated, and connected to the ground potential with a 10 Ω resistance. Therefore it is possible to easily determine the electron beam current by measuring the voltage. Additionally, the collector can be attached to other components, facilitating the extraction of ions for further measurements.

3.1.5 The injection system

Finally, the injection system works by using a needle valve that is attached to the FLASH-EBIT at a 90 °angle to the electron beam propagation axis, and connecting a gas cylinder to it. The needle valve is then used to set the pressure of injection. The injected compound then reaches the trap region via two-step differential pumping stages, permitting the regulation of the injection flow without significantly increasing the magnet chamber pressure of 10^{-10} mbar . The pressure of the first injection stage is set between 10^{-6} and 10^{-7}mbar, and the second stage is set between 10^{-8} and 10^{-9} mbar. The gas is collimated by various slits: the first slit is found between the two injection stages, the second is found before the gate valve that separates the injection system from the rest of the EBIT, the third and four slits are 5 mm apart and are found between the thermal shield and the magnet former.

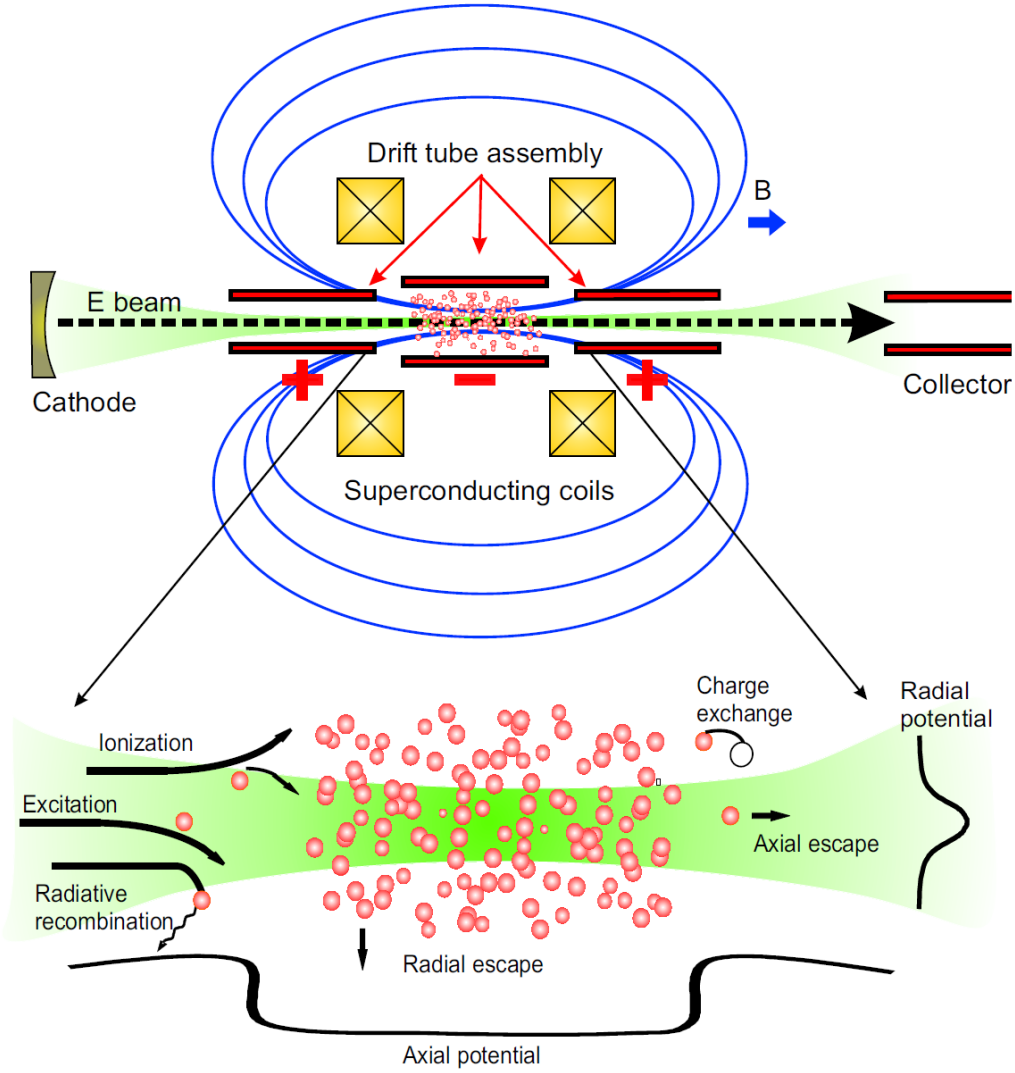

Figure 3.2: A schematic diagram of the principle of an EBIT and some of the processes occurring inside the trap. (from [22]).

3.2 Extreme ultraviolet spectrometer

An extreme ultraviolet (EUV) spectrometer developed by T. Baumann [23] is used to measure the EUV emitted by ions. Its main components are a reflective grating to disperse the light and a CCD camera (Charged Coupled Device) to record the spectrum. The spectrometer was kept under vacuum since EUV radiation is absorbed in air. A cross section of the spectrometer is seen in figure 3.3.

The functioning of the spectrometer is based on the Rowland circle: an illuminated point lying on the circumference of a circle with diameter R reflected by a concave grating of curvature with radius R will focus on this circle, provided that the centre of the grating also lies on the circle [24].

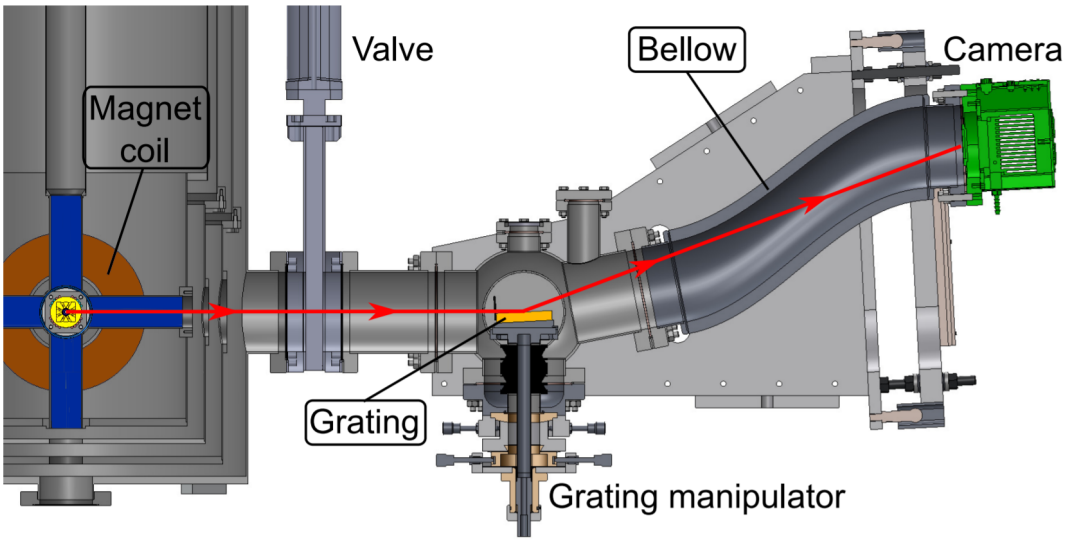

Figure 3.3: Cross section of the EUV spectrometer: EUV rays emanating from the ion cloud in the trap region are reflected by the grating and are focused on the CCD camera. The grating is mounted on the grating manipulator to fine-tune its vertical position. The bellow is used to reposition the camera, and a valve separates the spectrometer from the EBIT, so that the spectrometer can be detached without greatly affecting the pressure in the EBIT (from [25]).

3.2.1 The grating

The grating was manufactured by the company Hitachi to cover the EUV range. It is made from a 1200 lines/mm concave glass substance coated with gold to maximize reflectivity at near-grazing incidence. The grating is designed to focus on a plane, thus permitting a more compact spectrometer design. It has a curvature of radius $R = 13450$ mm and the dimensions $(40 \times 70 \times 12)$ mm^3 (see table 3.1 for more details). Its geometry can be changed using a grating manipulator which allows

repositioning along the x-, y- and z-planes, as well as the angle on incidence and the tilt of the grating, thus allowing precise focusing of the light onto the CDD camera.

Each vertical position in the focal plane corresponds to a different wavelength λ (see figure 3.4). This wavelength can be calculated geometrically by combining the diffraction equation (3.6) with a simple expression that stems from the configuration of the optical components. However, this method only constitutes a rough estimate of the wavelength position, as it assumes that the light is perfectly focussed on the camera, which is very unlikely.

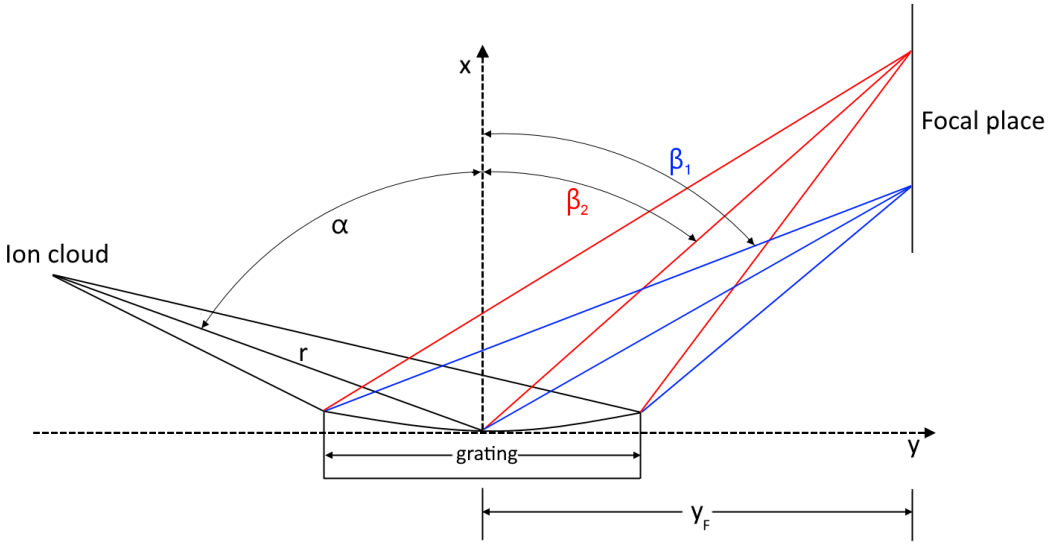

Figure 3.4: Diffraction of the emitted light for two different wavelengths. The angle of incidence is α and the diffraction angles β_1 and β_2 are the extreme angles for which the resulting image is still focussed correctly (from [15]).

The diffraction equation for a grating with groove separation d, angle of incidence α and angle β with respect to the focal plane is:

$$m\lambda = d(\sin\alpha - \sin\beta), \tag{3.6}$$

where m is the order of diffraction.

From figure 3.4 we can easily see that the following expression holds:

$$\tan(90^\circ - \beta) = \frac{x}{y_\mathrm{F}}, \tag{3.7}$$

where x is the vertical position of the focused light and y_F is the distance from the centre of the grating to the focal plane.

To determine x, we need the position of the camera x_camera (which was 155 mm for the present experiment) and the line pixel position of interest x_Pix (between 1 and 2048). Additionally, the positions $x_\mathrm{camera,0}$ and $x_\mathrm{Pix,0}$ for $m = 0$ (zeroth order) have to be found.

Table 3.1: Properties of the near-grazing-incidence grating given by the manufacturer.

Part number	Grooves per mm	R (mm)	Blaze WL (nm)	α (°)	β_1 (°)	β_2 (°)
001-0660 *3	1200	13450	9	87	-83.04	-75.61

Dimensions H×W×T (mm^3)	r (mm)	L (mm)	Blaze angle (°)	y_F (mm)	$\lambda_1 - \lambda_2$ (nm)	Material
40×70×12	564	75.73	3	563.2	5 - 25	BK7

Now we can combine equations (3.6) and (3.7) to find the wavelength of the recorded spectra for a single pixel position x_{Pix}:

$$\lambda(x_{\text{Pix}}) = d\left[\sin\alpha - \sin(90° - \arctan\frac{x}{y_F})\right], \text{with} \tag{3.8}$$

$$x = \frac{x_{\text{Pix}}}{2048}\cdot 27.6\text{mm} + x_{\text{camera}} - \left(x_{\text{camera},0} + \frac{x_{\text{Pix},0}}{2048}\cdot 27.6\text{mm} - 29.5\text{mm}\right), \tag{3.9}$$

where 27.6 mm corresponds to the CCD sensor width and the calculated value for the 0th order is 29.5 mm.

3.2.2 CCD Camera

The CCD Camera used is from the Andor company. It can be repositioned using the bellow, which enables a wider range of wavelength measurements, since each position in the camera will be illuminated by light rays of different wavelengths.

Its CCD chip has an area of (27.6 × 27.6) mm^2 with 2048 × 2048 pixels, meaning that each pixel has an area of (13.5 × 13.5) μm^2. The chip is back-illuminated, meaning that the light rays are absorbed by the readout electronics after they reach the camera, not before, as would be the case in a front illuminated camera. This increases the amount of light captured, thus improving the signal-to-noise ratio. Each photon that reaches the chip causes an electron to be emitted towards the readout electronics, which consist of an analogue to digital converter (ADC). However, the conversion rate is limited to 0.7 counts per electron on average [15].

The line intensities of the observed spectra depend on the emission strength and the ion population, meaning that a higher number of ions corresponds to larger line intensities. Yet they also depend on the spectrometer efficiencies, such as the grating response and the detector efficiency. Figure 3.5 clearly showcases an overall decrease in the total relative spectrometer response with an increasing wavelength, going from about 20 % to 5 %.

Dark current poses a challenge in observing the signal. The dark current stems from charges generated in the detector when no outside radiation is present. It is

caused by random generation of electrons and holes within the depletion region of the device. The camera is cooled down to $-70°$ C with a Peltier element in order to counteract the dark noise as much as possible.

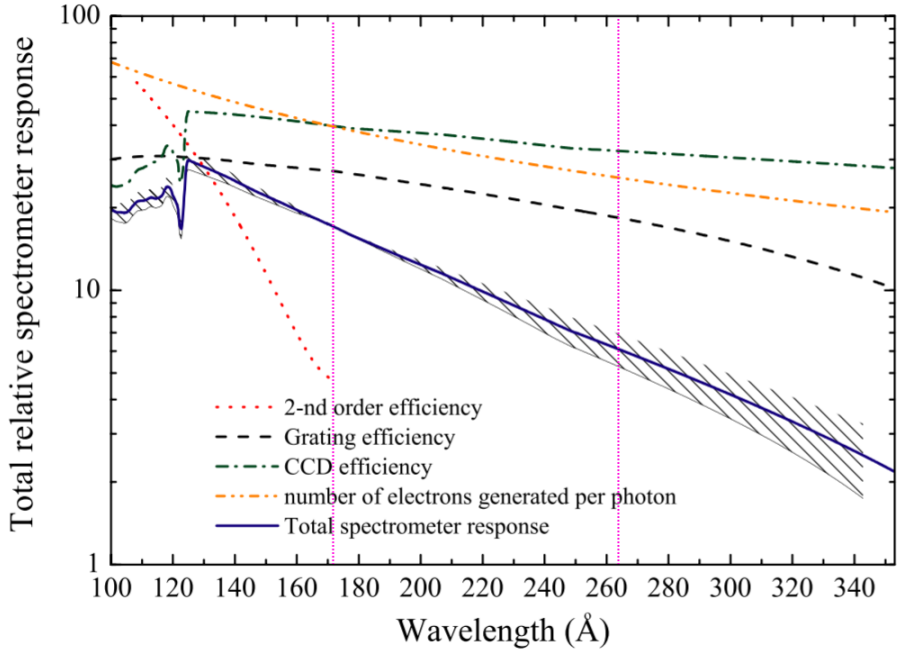

Figure 3.5: Total relative spectrometer response as a function of the photon energy. The second-order diffraction, grating and CCD efficiencies are shown , as well as the number of electrons generated per photon and the total spectrometer response. The wavelength range we measured is marked with dotted pink lines (modified from [26]).

4 Spectroscopy of Ruthenium ions in the Extreme Ultra-Violet (EUV) regime

4.1 The measurement

Ruthenium ions were trapped at the FLASH-EBIT, which were mainly produced through electron impact ionization. The compound Tris(2,2,6-6tetramethyl-3,5-heptanedionato) ruthenium(III) ($C_{33}H_{57}O_6Ru$) was injected continuously into the trap at a pressure of 2.9×10^{-7} mbar. Since this compound is a solid at room temperature, the injection system was heated to 40 – 45 °C. The sublimation point (vapour pressure) of ruthenium is at a pressure of 1.2 mbar.

Before starting with the measurement the camera height was adjusted to 155 mm, which corresponds to wavelengths between 17 and 26 nm. Then eleven measurements with 1800 seconds of exposure were taken over a range of 200 eV at 20 eV intervals, starting at a beam energy of 240 eV and ending at a beam energy of 440 V. Background measurements achieved by inverting the trap were also recorded for each spectrum. The background measurements are then easily subtracted from the main measurements by using the Arithmetic Operations feature in the *Andor Solis* software. A short summary of the operational parameters can be found in table 4.1.

It is important to note that calibration measurements using iron were taken *before* measuring with ruthenium, which led to some iron build up in the injection system. This over abundant iron was removed by heating the injection system to 150 °C and periodically checking to see if the iron lines diminished. Therefore, special care was taken in the data analysis to ensure that the ruthenium spectra were free of iron lines.

Table 4.1: Operational parameters of the FLASH-EBIT for the results presented in this thesis.

Parameter	Value
Electron beam current	15 mA
Depth of the trap potential	100 V
Energy range	240 - 440 V
Pressure of gas injector	2.9×10^{-7} mbar
Temperature of injection system	40 °C
Beam radius	25 μm
Trap length	50 mm
Magnetic Field	6 T

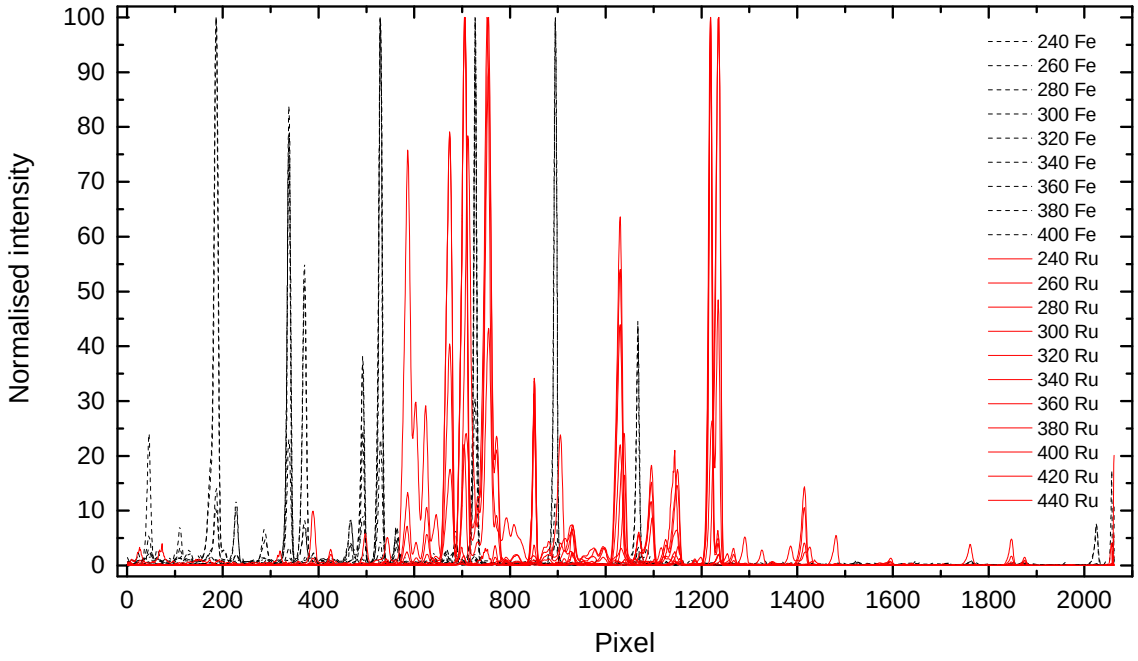

Figure 4.1: Comparison between the peaks when iron and ruthenium ions were injected. Both measurements were taken at the same electron beam energy range as well as at the same camera height of 155 mm. The iron peaks are represented with the dashed black lines and the ruthenium peaks with the solid red lines. The numbers in the legend represent the uncorrected beam energy followed by the ionic species.

4.2 Preliminary line identification of Ru-ions

Before the process of identifying the ruthenium lines could be started, it was essential to confirm the presence of Ru in the trap, and in particular the absence of other species in the spectra. In order to verify that there were not any peaks coming from trace iron atoms (that could potentially still found in the injection system after taking the calibration measurement) the data for each beam energy was plotted for iron and ruthenium (see Figure 4.1). Hence, it was demonstrated that there is no overlap between the major lines of iron or ruthenium. A small overlap was observed at the very end of the spectra, at pixel position 2058 and these peaks were therefore excluded from the line identification.

The presence of other lines from the impurity ions emitted from the cathode, such as barium and tungsten, was also ruled out by comparing measurements taken with a closed injection valve to the EBIT. The closed injection valve measurements contained very few lines, none of which matched the ruthenium spectral lines. The absence of any contaminants from other species was thus confirmed with a reasonable degree of certainty.

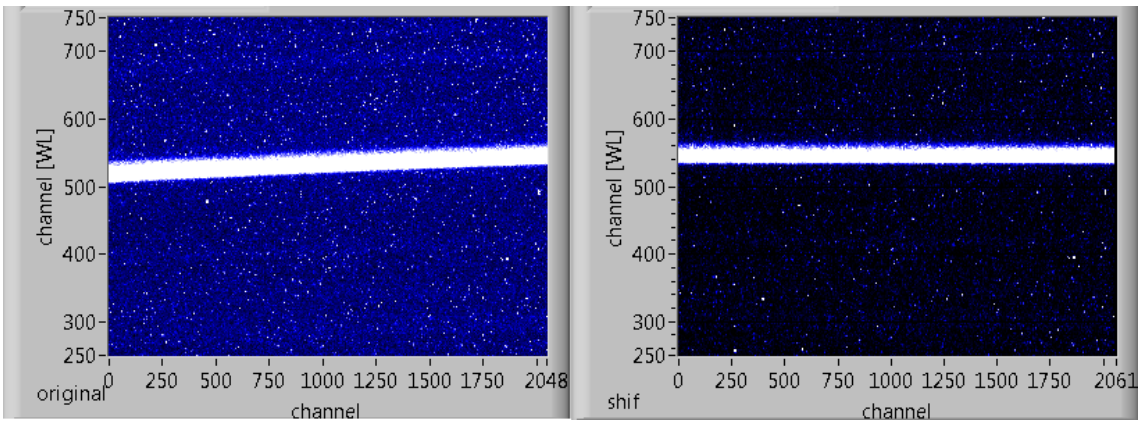

Figure 4.2: Left: Original image. Right: Shifted image using ShiftMatrix. Cosmic rays and background are removed with upper and lower level discriminators.

4.3 Corrections to the spectrum

The data retrieved from the EUV spectrometer needs to be corrected before it can be analysed, since the CCD camera position is not completely parallel to the horizontal axis of the grating, meaning that the images taken with the CCD camera are slightly shifted to one side.

In order to straighten the image, a program called ShiftMatrix was used (developed in LabVIEW by M.C. Simon). ShiftMatrix translates the pixel positions according to a parabolic function [25]:

$$x_{\text{straight}} = x_{\text{original}} + b \cdot y + c \cdot y^2, \tag{4.1}$$

where the parameters b and c are selected to return straight lines that are parallel to the reference lines given by the program (see fig. 4.2). These lines therefore have the smallest line widths and the optimal resolution. Shiftmatix is also used to remove any remaining background and cosmic rays, with a lower level discriminator (LLD) and an Upper level discriminator (ULD) respectively. These parameters are selected so as to reduce the offset in the y-projection as much as possible. To make the shifting process faster, the program ShiftBatch can also be used, where the same parameters are input for several data and these are shifted automatically. However, it is important to use this feature sparingly, since the parameters can change significantly depending on the signal-to-noise ratio of the spectra.

The shifted data can be saved as a 1D or 2D in ASCII format, where the one dimensional file consists of a y-projection of the 2D image. Shifting the image has the unwanted numerical consequence of slightly altering the pixel location for each image, depending on which shifting parameters were used. Thus, an extrapolation of the data is made in Origin software, starting at a value of 0 and ending with 2061. This guarantees that all the shifted data is comparable.

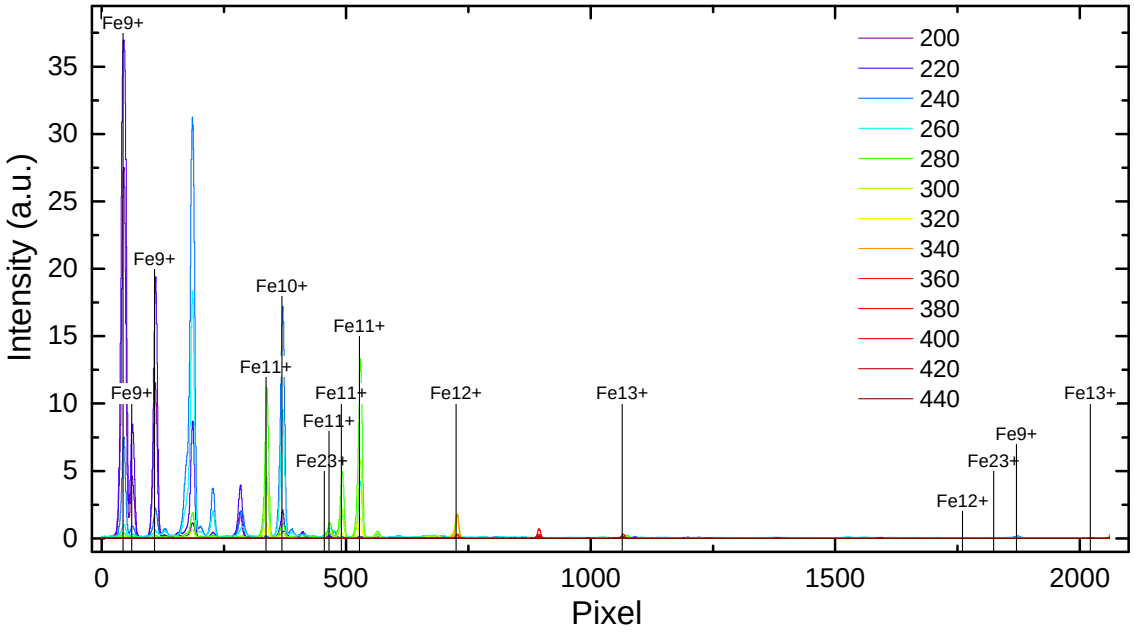

Figure 4.3: Iron ion lines used in the calibration were identified with the NIST atomic spectra database. The coloured lines correspond to the electron beam energies numbered in the legend.

4.4 Spectral calibration

The calibration was made by relying on the fact that the wavelength range of the recorded spectra is constant if the camera and grating positions remain unchanged (independent of the electron beam energy or the ions in the trap). Consequently, we injected the compound iron pentacarbonyl ($Fe(CO_5)$) into the FLASH-EBIT and measured at energies between 200 and 440 eV. The spectra produced at these energies have well known lines in the ultraviolet regime.

First, we removed the background and corrected the images using ShiftMatrix. Then the shifted data was imported into Origin and a rough calibration of the wavelength was made using the geometric properties of the spectrometer, as explained in section 3.2.1. Using the rough calibration as guidance, several peaks were identified with data from the National Institute of Standards and Technology (NIST) [27]. We then fitted the peaks with a Gaussian function and obtained the centroid of each peak. The NIST theoretical data was already benchmarked previously by Liang *et al.* [20] which makes it reliable to use for the present experiment. Finally, we plotted the identified wavelengths against the pixel number and carried out the calibration by fitting a second order polynomial equation to the data (showcased in table 4.2):

$$y = a + b \cdot x + c \cdot x^2, \tag{4.2}$$

where y is the wavelength in nm, x is the pixel number, a is the intercept at the y-axis, and b and c are the fitting coefficients.

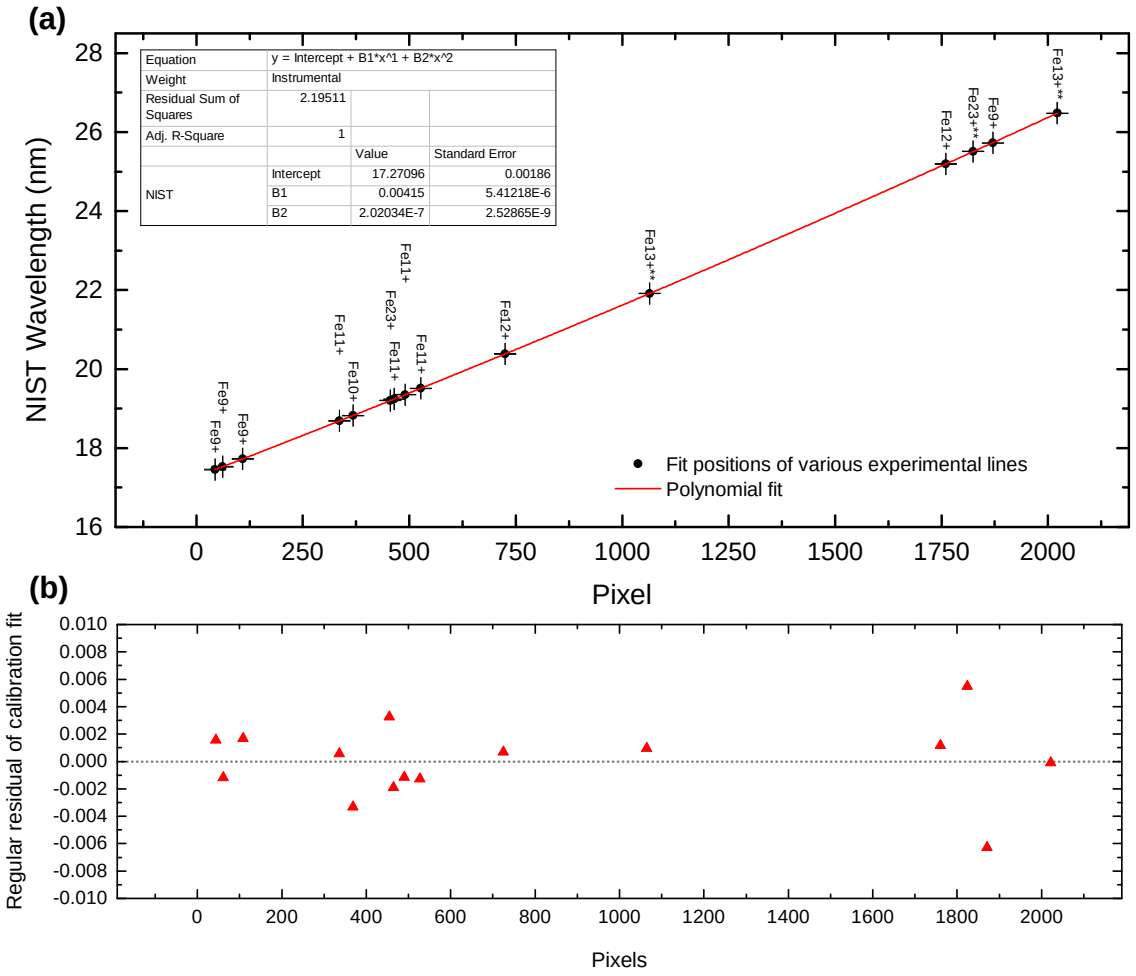

Figure 4.4: (a) Polynomial fit used for calibration at 155 mm camera height. Iron wavelengths are taken from NIST [27]. (b) Residual of the polynomial fit. The residual plot suggests a goodness of fit, which is supported by the Adj. R-squared value of 0.999.

The following values were computed for the fit coefficients:

$$a = 17.2709, \quad b = 0.00415, \quad c = 2.02 \times 10^{-7}, \tag{4.3}$$

with the errors:

$$\Delta a = 0.00184, \quad \Delta b = 5.3 \times 10^{-6}, \quad \Delta c = 2.50 \times 10^{-9} \tag{4.4}$$

The polynomial fit used for calibration and its residuals are shown in figure 4.4. Qualitatively, the residual plot shows a statistical fluctuation of the values around zero, and no apparent bias in any direction. This is corroborated by the adjusted R-Square value of 0.999, which indicates goodness-of-fit check. Nevertheless, we made the decision to use the uncalibrated data to find the centroid of the peaks for

the Ru-ion lines. This is because the calibration was quite sensitive to the number of data points used for fitting, with the intercept varying on a scale of about ± 0.02. A change of that magnitude results in a difference of about 0.05 nm in the final result, which certainly affects the accuracy of the measurement. The line positions were thus first extracted in pixel units, and then calibrated to yield the wavelength positions. The original pixel locations of the lines are given in tables $6.1 - 6.9$ to be able to easily change the calibration factor if necessary.

The conversion of pixel positions to wavelength positions is trivial: equation (4.2) and the polynomial fit coefficients are used. In order to convert the error from pixels to wavelength, we used the principle of error propagation:

$$\Delta y = \sqrt{(\Delta a)^2 + (x \cdot \Delta b)^2 + (x^2 \cdot \Delta c)^2 + ((b + 2cx) \cdot \Delta x)^2} \tag{4.5}$$

Table 4.2: Spectral calibration values for 155 mm of camera height: pixel positions for several peaks were allocated to their corresponding wavelengths λ and charge states. The errors are given by ΔPixel and $\Delta\lambda$. The values for λ were taken from the NIST database [27].

Pixel	ΔPixel	λ (nm)	$\Delta\lambda$ (nm)	Charge state
43.539	0.029	17.453	0.007	Fe^{9+}
61.765	0.107	17.527	0.007	Fe^{9+}
108.380	0.058	17.724	0.007	Fe^{9+}
336.169	0.035	18.688	0.007	Fe^{11+}
368.306	0.031	18.822	0.007	Fe^{10+}
455.160	0.080	19.203	0.007	Fe^{23+}
464.759	0.399	19.239	0.007	Fe^{11+}
490.284	0.079	19.351	0.007	Fe^{11+}
527.308	0.030	19.512	0.007	Fe^{11+}
724.813	0.083	20.383	0.007	Fe^{12+}
1064.434	0.155	21.914	0.007	Fe^{13+}
1760.207	0.195	25.195	0.007	Fe^{12+}
1824.212	0.202	25.511	0.007	Fe^{23+}
1870.544	0.116	25.726	0.007	Fe^{9+}
2021.824	0.221	26.479	0.007	Fe^{13+}

4.5 Charge state identification

The one dimensional ASCII files were imported into the Origin software and the intensities for three equivalent measurement cycles were added. A 2D plot was then made (see figure 4.6). To find the charge states of the ruthenium ions, several vertical contour profiles were made along the most prominent Ru-ion lines. These profiles of the line intensities at specific wavelengths were plotted against the electron beam energy in figure 4.5. Ionization energies were added to the plot in order to estimate where each charge state starts. Doing this provides a clear picture of the evolution of the line intensities, and makes it easier to distinguish between charge states according to their energies. The ionization energies used were taken from the Scofield and NIST databases and are showcased in table 4.3. These values are later confirmed by the flexible atomic code (FAC) calculations [28]. It must be noted that the uncorrected electron beam energy was used, which limits the quantitative analysis of this plot, but it still provides sufficient data to make a preliminary allocation of the ionic charge states.

The composite and smoothed image of the ruthenium spectra obtained at electron beam energy intervals of 20 eV is shown in figure 4.6. The appearance and later disappearance of certain lines at certain electron beam energies is evident to see. For example, there are a number of lines that start at an energy below 240 eV and end at 320 eV in figure 4.6. A similar energy range can be seen in figure 4.5 for lines peaking at 260 eV, in between charge states 11+ and 12+. This gives a clear signature of the changing charge states of the Ru-ions.

The agreement between the observed spectra and synthetic spectra, presented in the next chapter, boosts our confidence in the identification of correct charge states.

Table 4.3: Ionization energies for several Ru-ion charge states observed in the present experiment. Ionization energies (I_p) were taken from the Scofield and NIST databases [27, 29].

Charge state	NIST I_p (eV)	Scofield I_p (eV)
Ru^{8+}	178.4(5)	178.5
Ru^{9+}	198.0(2)	200.1
Ru^{10+}	219.9(2)	222.2
Ru^{11+}	245.0(3)	244.8
Ru^{12+}	271.0(3)	273.0
Ru^{13+}	295.9(9)	296.9
Ru^{14+}	348.0(3)	353.6
Ru^{15+}	376.3(1)	379.7
Ru^{16+}	670.0(3)	673.3

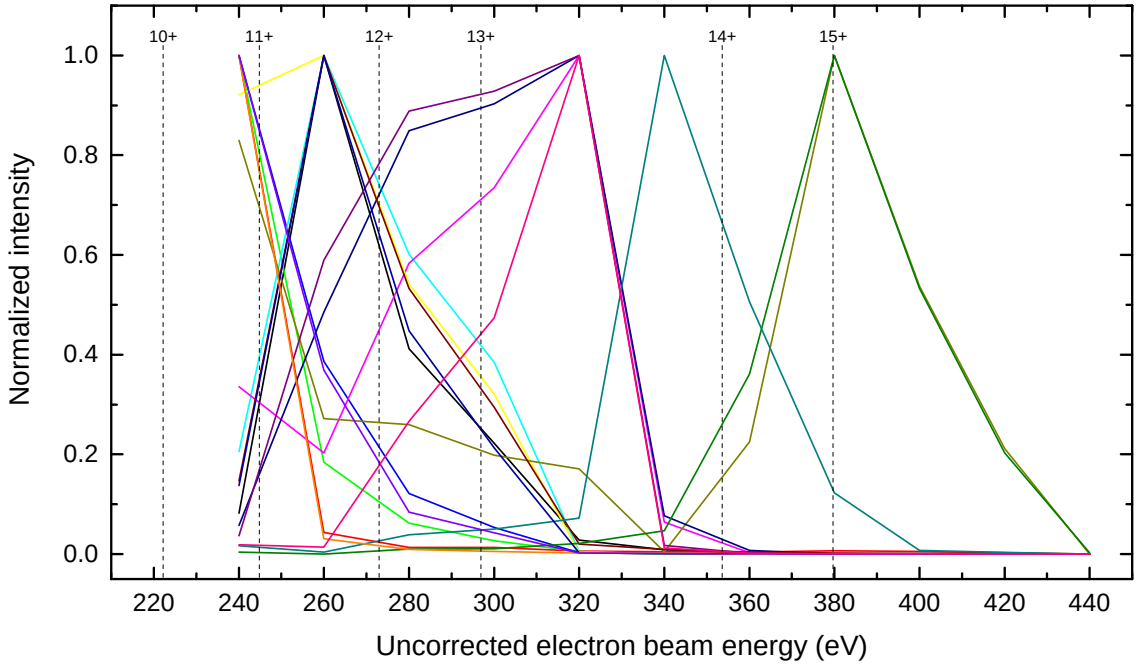

Figure 4.5: Evolution of the line intensities for several ruthenium ion as a function of the uncorrected electron beam energy. The ionization energies of ruthenium ions are shown with the dashed lines.

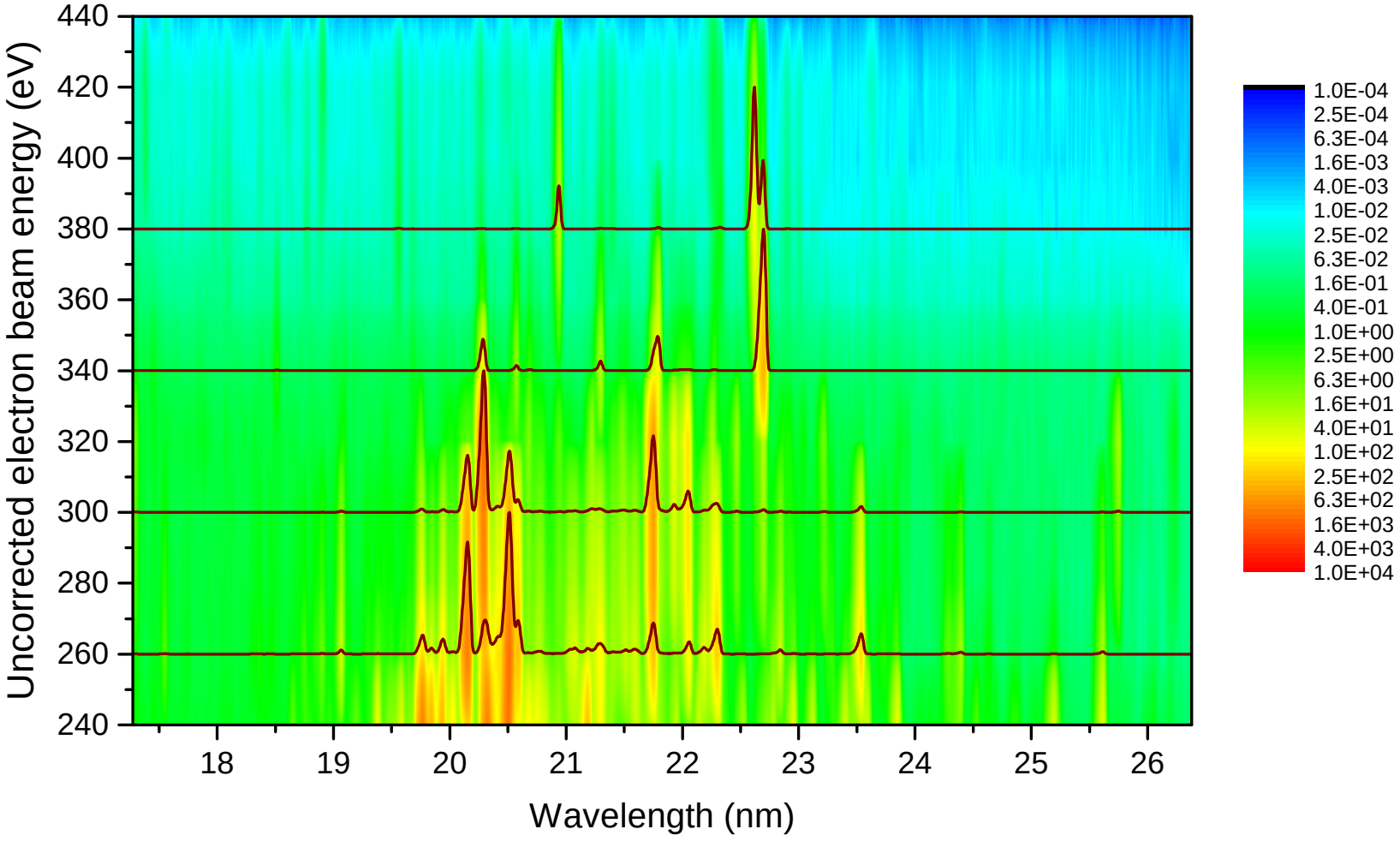

Figure 4.6: Two dimensional representation of spectra from Ru-ion in the wavelength range 17.3 and 26.4 nm. The red curves represent the one-dimensional plot at corresponding electron beam energies on the y-axis.

5 EUV data of Ru^{14+} and Ru^{15+}

As was mentioned in the previous chapter, the calibration and the identification of the different charge states of the ruthenium ions were accomplished. Due to time constraints, we focus on two of these charge states in this thesis.

In this chapter, we showcase the EUV spectra taken for Ru^{14+} and Ru^{15+} ions. These specific charge states were selected from the 2D plot (figure 4.6) according to their ionization potentials. The dark red curves at the electron beam energies of 340 eV and 380 eV represent the spectra for these two charge states.

In figures 5.1 and 5.2, the intensity is plotted as a function of the wavelength by projecting the observed CCD image on to the wavelength axis. The same line graphs are shown twice, with the only difference being that the top graph has a linear scale, whereas the bottom graph has logarithmic scale. This was done in order to make smaller peaks more visible at first glance. Additionally, numbered labels were added to the studied peaks to easily find them.

We extracted the line positions (wavelengths) by fitting multiple Gaussians to the observed spectra. In the fitting procedure, the line centroids, amplitudes, and the widths were set as a free parameters, while the offset was fixed to zero. The extracted line positions for Ru^{14+} and Ru^{15+} are given in tables 5.1 and 5.2 in pixels as well as in wavelengths. This facilitates the future analysis of the data should the calibration factors improve slightly. This improvement can be done with the identification of more iron lines from the same datasets. The obtained wavelengths from Ru^{14+} and Ru^{15+} spectra are later compared with the theoretical calculations carried out with the flexible atomic code (FAC) developed by Ming Feng Gu [28].

It should be noted that while the number of lines observed in the present experiment is exhaustive, we still provide a complete table with observed wavelength values for the future line identification to benchmark theoretical calculations and astrophysical models. These tables and the spectra are represented in the appendix.

Table 5.1: Peak positions at an electron beam energy of 340 eV. L represents the label number in figure 5.1, Pixel and ΔPixel are the peak positions in pixel and its error, and λ and $\Delta\lambda$ are the wavelength position and its error in nm.

L	Pixel	ΔPixel	λ (nm)	$\Delta\lambda$ (nm)
1	295.280	0.234	18.514	0.003
2	565.769	0.210	19.684	0.004
3	702.676	0.078	20.287	0.004
4	767.627	0.108	20.576	0.005
5	792.914	0.461	20.689	0.005
6	928.646	0.076	21.299	0.006
7	1035.274	0.186	21.784	0.006
8	1086.807	0.263	22.020	0.007
9	1143.086	0.218	22.279	0.007
10	1233.425	0.164	22.697	0.008

Table 5.2: Peak positions at an electron beam energy of 380 eV. L represents the label number in figure 5.2, Pixel and ΔPixel are the peak positions in pixel and its error , and λ and $\Delta\lambda$ are the wavelength position and its error in nm.

L	Pixel	ΔPixel	λ (nm)	$\Delta\lambda$ (nm)
1	538.142	0.154	19.563	0.004
2	566.032	0.567	19.685	0.004
3	698.527	0.321	20.268	0.005
4	767.381	0.326	20.575	0.005
5	793.464	0.931	20.691	0.006
6	849.157	0.052	20.941	0.005
7	929.387	0.234	21.302	0.006
8	951.403	0.356	21.402	0.006
9	1037.845	0.154	21.796	0.006
10	1152.753	0.212	22.323	0.007
11	1217.488	0.049	22.623	0.008
12	1233.395	0.107	22.697	0.008
13	1277.985	0.247	22.905	0.008
14	1300.925	0.464	23.012	0.009

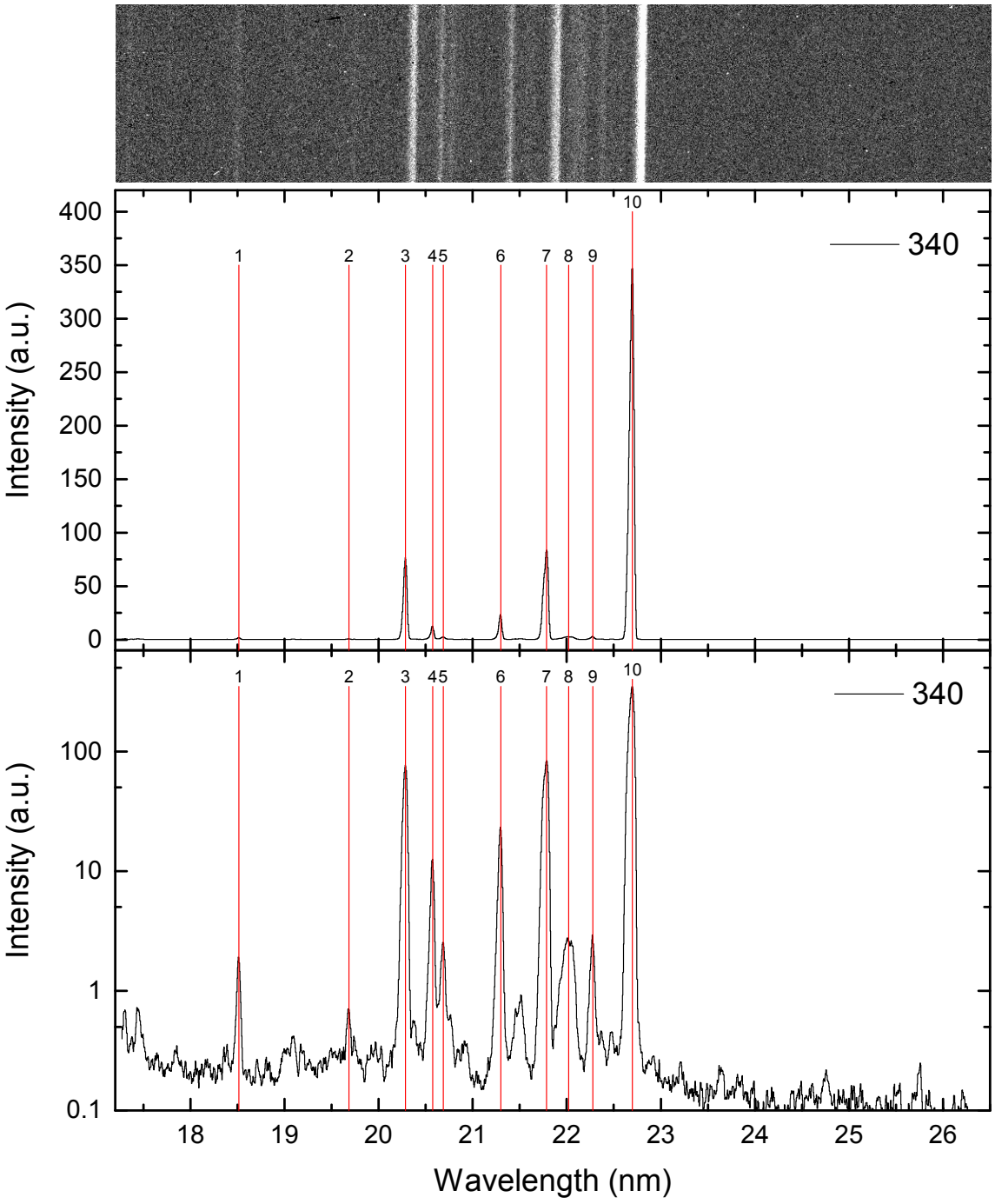

Figure 5.1: Ru-ion peaks at E_{beam}=340 eV. Peak centroids are shown with the labelled red lines.

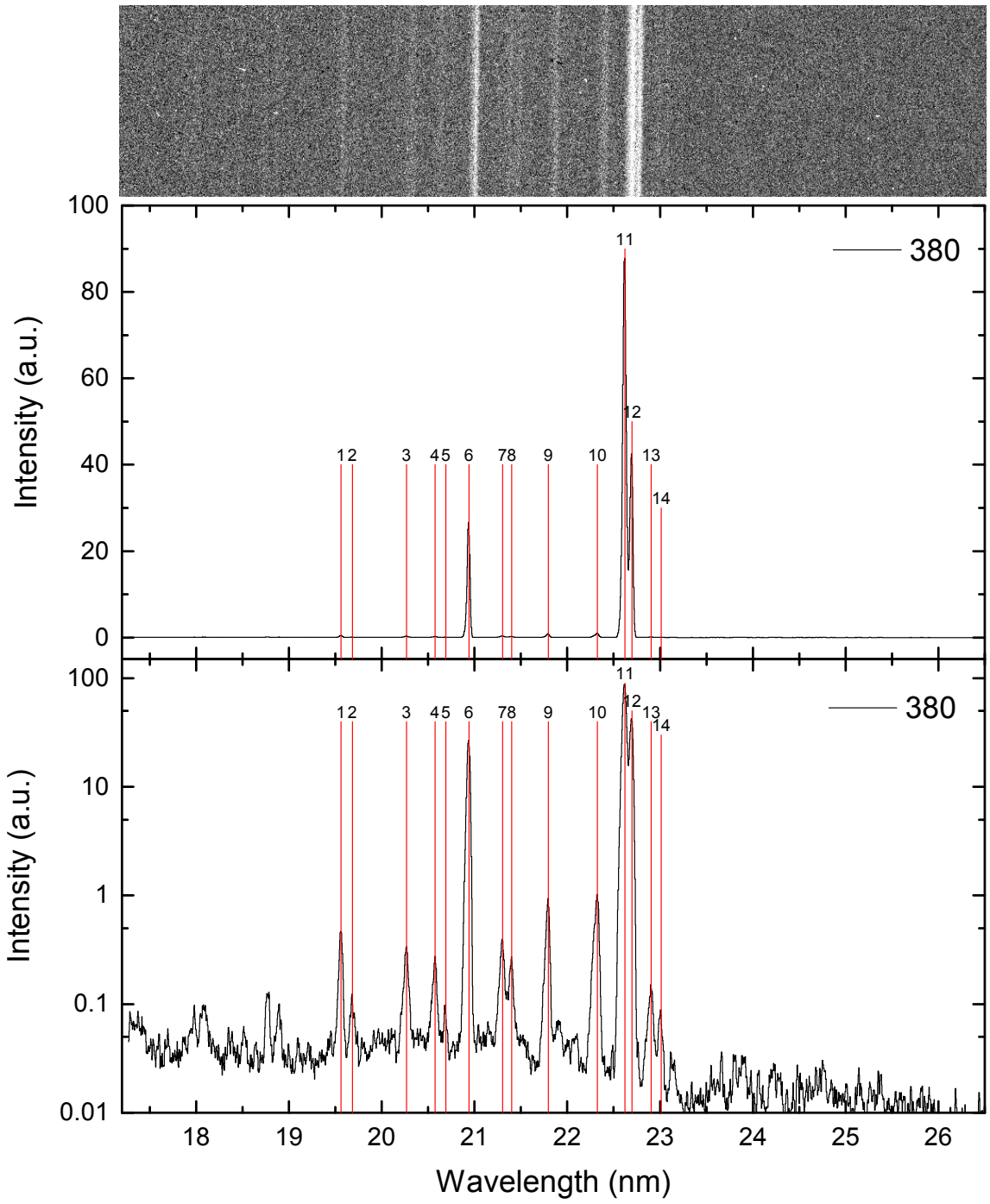

Figure 5.2: Ru-ion peaks at E_{beam}=380 eV. Peak centroids are shown with the labelled red lines.

5.1 Comparison with theory

In this section we compare the experimental results obtained for Ru^{14+} and Ru^{15+} ions with advanced theoretical calculations carried out with the FAC code. The theoretical calculations were provided by C. Shah. Since no theoretical data are available from NIST for these specific charge states of Ru, completely new calculations had to be performed in order to identify the lines.

First, the energies and transition probabilities are computed. The observed energy range in the present experiment is in between 50 – 70 eV, which represent the intra-shell n=4 shell transitions in Ru-ions. Most of the dominant electronic transitions are occurring between $4s$, $4p$, $4d$, and $4f$ sub-shells. With this first step we were able to assign some of the lines in the observed spectra with the predictions. However, the observed spectra do not show the predicted large numbers of transitions. Therefore, we had to make a collisional radiative modelling which accounts for the excitation processes caused by a monoenergetic electron beam in the EBIT and the branching ratio of various radiative decay channels.

To make collisional radiative modelling (CRM), we calculated energy levels, radiative transition probabilities, electron impact excitation, and de-excitation cross sections using FAC. In the calculations, we consider $1s$, $2s$, $2p$, $3s$, $3p$, and $3d$ shells as closed shells, which means that no electronic excitation shall be made from those shells. The ground states of the Ru^{14+} and Ru^{15+} ions are $4s^2$ and $4s^1$, respectively. In addition to the ground state configurations, all possible excitation configurations within the $n = 4$ shell were included in the calculations. For completeness, we include an electron to $5s$, $5p$, and $6s$ shells in CRM. The radiative cascades from such high-n states were also taken into account. Inclusion of all of these states return more than 100 possible electronic configurations for both charge states. The calculated transition rates and cross sections are used in CRM to numerically solve the quasi-stationary-state rate equations.

In CRM, we have selected an electron density of 10^{10} cm^{-3}. The electron beam density in the trap is roughly estimated from the iron lines used in the calibration. A few of the observed iron lines are sensitive to the electron density in the EBIT, and by taking the intensity ratio between them, we have extracted the effective electron beam density in an EBIT. More details regarding to such estimation is given by Liang *et al.* [26] . The electron energy distribution was set to follow Gaussian distribution with a centroid at 340 and 380 eV for the Ru^{14+} and Ru^{15+} ions, respectively. The Gaussian distribution has a width of 5 eV, and has a cut off $\pm$ 10 eV from the centroid position. With these parameters, we solved the rate equations, which returned the line strengths corrected for the energy level population distribution and quenching of transitions by electron impact [25]. Based on the corrected line strengths from CRM calculations, we have produced the synthetic spectra (convolved with the experimental line widths) to compare with the experimental data.

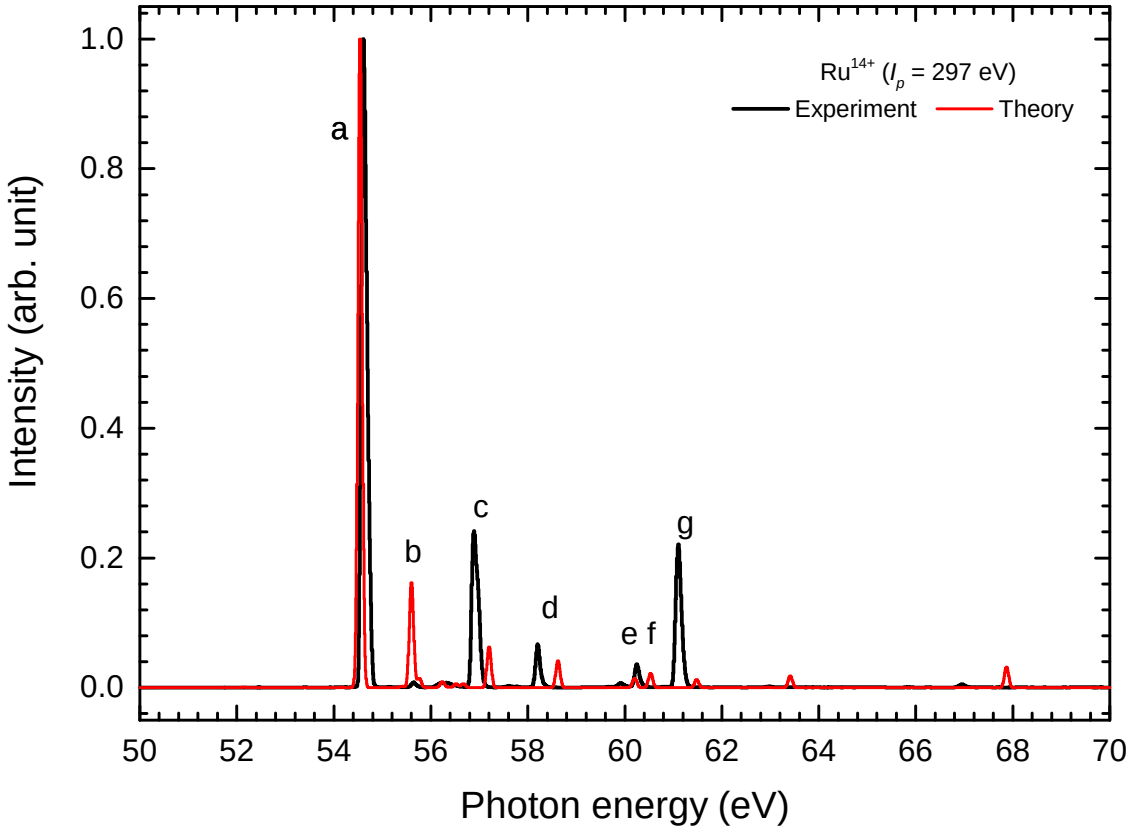

Figure 5.3: Comparison between experimental and theoretical Ru^{14+} spectra. The lines from the experiment and theory are shown in black and red, respectively. Identified transitions are listed from a) to g). The theoretical calculations were obtained with FAC.

In figure 5.3 the spectrum for Ru^{14+} is shown, with the black line representing the experimental spectrum, and the red line representing the spectrum based on FAC calculations. Seven peaks are identified, listed from a) to g), and their electronic transitions are shown as a Grotrian (or term) diagram in figure 5.4.

From figure 5.3 we can qualitatively observe that line a) has a relatively good agreement with the theory, especially regarding the intensity. There is also good agreement in the photon energies. Line b) has the best agreement with the theory in terms of photon energy, but its intensity, and therefore radiative rate, is much lower than expected. Line c) shows the opposite behaviour, with the experimental intensity being considerably higher than the prediction. Peaks d), e) and f) have the expected intensities, but are increasingly shifted from their theoretical counterparts. Line g) shows similar characteristics to lo line c), having much higher radiative rates than expected.

It also becomes apparent that the experimental lines are shifted to the right of the theory for line a) and b), and are then shifted to the left of the theory from lines c) to g). This shift can thereby not be described as a linear translation.

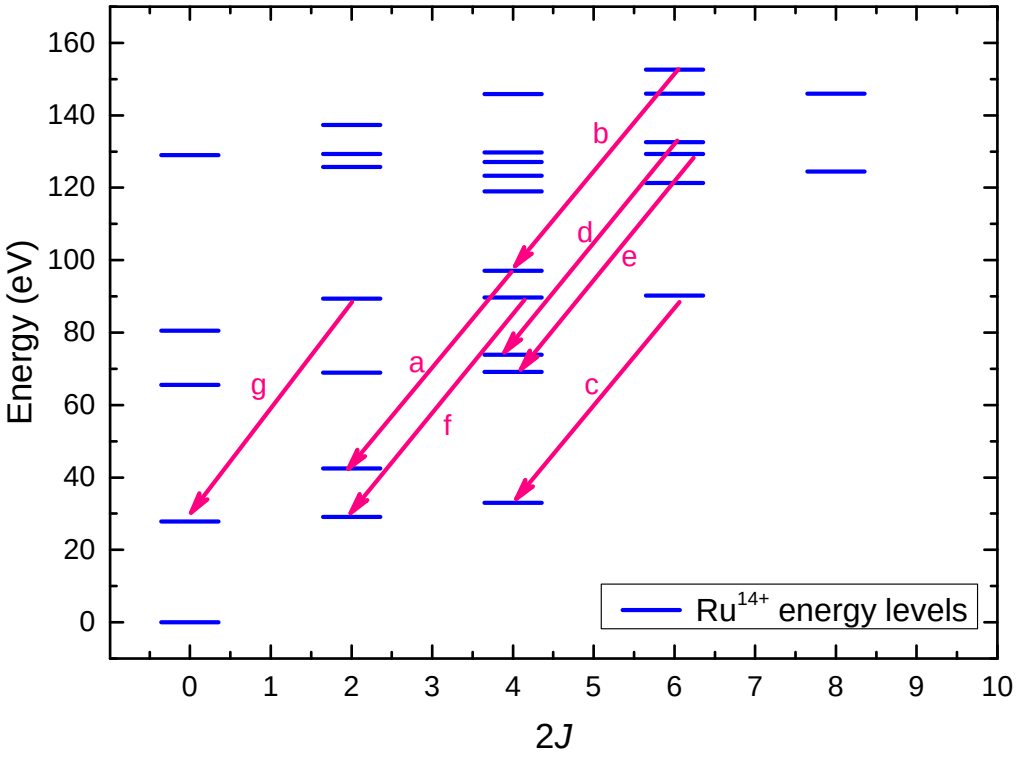

Figure 5.4: Grotrian level diagram of the energy levels of Ru^{14+} as obtained with FAC. The identified transitions are indicated with arrows and listed from a to g. The values corresponding to the transitions are found in table 5.3.

Table 5.3: Identified lines in the charge state 14^+. L is the label shown in figure 5.3, LL and UL are the lower and upper energy levels of the transition, respectively. E_{photon} is the theoretical photon energy. $\Delta(\lambda)$ is the difference between the theoretical and experimental wavelength positions.

L	LL	UL	E_{photon}	Wavelength (nm)		$\Delta(\lambda)$
			(eV)	Experiment	Theory	(nm)
a	$[4s_{1/2}4p_{3/2}]_1$	$[4s_{1/2}4d_{5/2}]_2$	54.554	22.697(8)	22.727	0.030
b	$[4s_{1/2}4d_{5/2}]_2$	$[4s_{1/2}4f_{7/2}]_3$	55.612	22.279(7)	22.294	0.015
c	$[4s_{1/2}4p_{3/2}]_2$	$[4s_{1/2}4d_{5/2}]_3$	57.219	21.784(6)	21.668	-0.116
d	$[4p^2_{3/2}]_2$	$[4p_{3/2}4d_{5/2}]_3$	58.635	21.299(6)	21.145	-0.154
e	$[4p_{1/2}4p_{3/2}]_2$	$[4p_{3/2}4d_{5/2}]_3$	60.205	20.689(5)	20.594	-0.095
f	$[4s_{1/2}4p_{1/2}]_1$	$[4s_{1/2}4d_{3/2}]_2$	60.547	20.576(5)	20.477	-0.099
g	$[4s_{1/2}4p_{1/2}]_0$	$[4s_{1/2}4d_{3/2}]_1$	61.496	20.287(4)	20.161	-0.126

The reason for this discrepancy between the experimental and the predicted data could stem from various sources. As previously mentioned, the calibration used for the Ru-ion spectra is very sensitive to small changes, and there is the possibility that the second calibration parameter is slightly higher or lower than it should be. Other possible reasons are the theoretical predictions themselves, due to the high

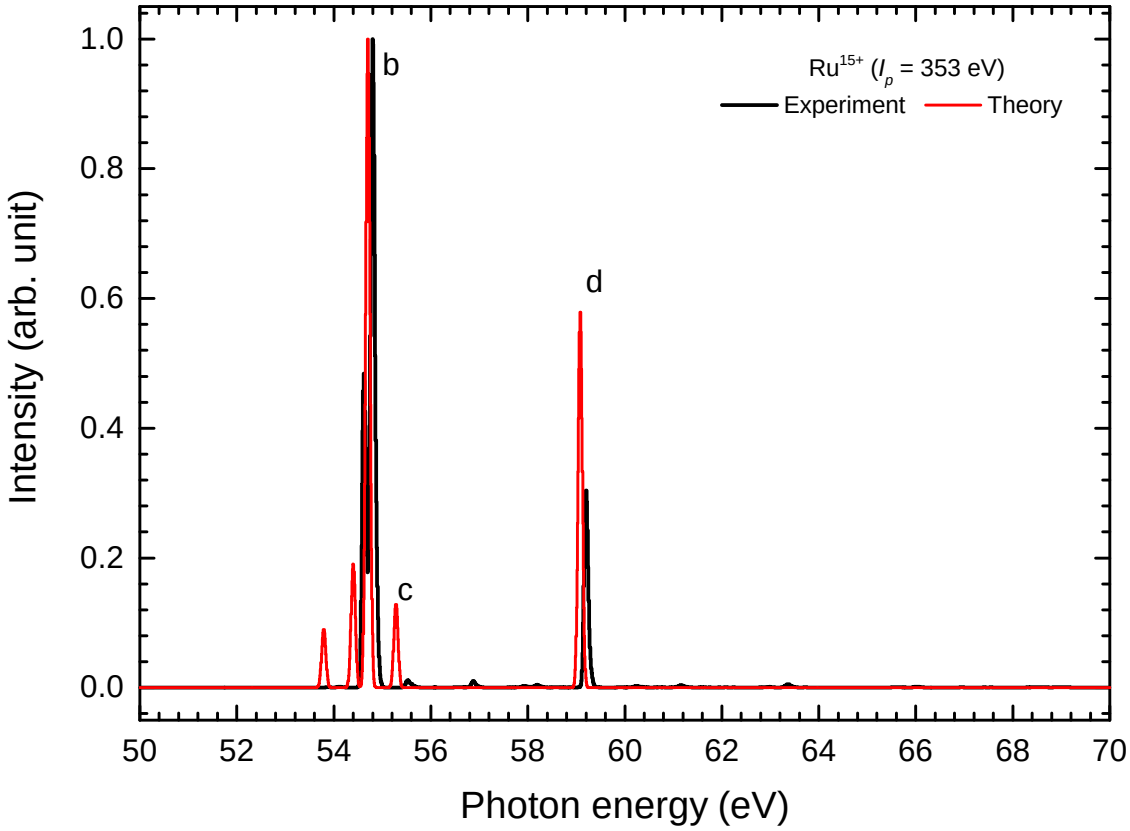

Figure 5.5: Comparison between experimental and theoretical Ru^{15+} spectra. The lines from the experiment and theory are shown in black and red, respectively. Identified transitions are listed from b) to d). The theoretical calculations were obtained with FAC.

number of electrons, the calculations become more complex, and thus less accurate. It has been previously established that different theories have disagreement with each other as well as with experiments [25, 30]. It should also be noted that the effective electron beam density in the trap could vary over time with different charge states abundances. This would result in change of intensities. Hence, currently, no conclusive reason can be given to fully explain the observed discrepancies.

Table 5.4: Identified lines in the charge state 15^+. L is the label shown in figure 5.5, LL and UL are the lower and upper energy levels of the transition, respectively. E_{photon} is the theoretical photon energy. $\Delta(\lambda)$ is the difference between the theoretical and experimental wavelength positions.

L	LL	UL	E_{photon} (eV)	Wavelength (nm) Experiment	Theory	$\Delta(\lambda)$ (nm)
b	$4p_{3/2}$	$4d_{5/2}$	54.715	22.623(8)	22.660	0.037
c	$4d_{3/2}$	$4f_{5/2}$	55.300	22.323(7)	22.420	0.097
d	$4p_{1/2}$	$4d_{3/2}$	59.096	20.941(5)	20.980	0.039

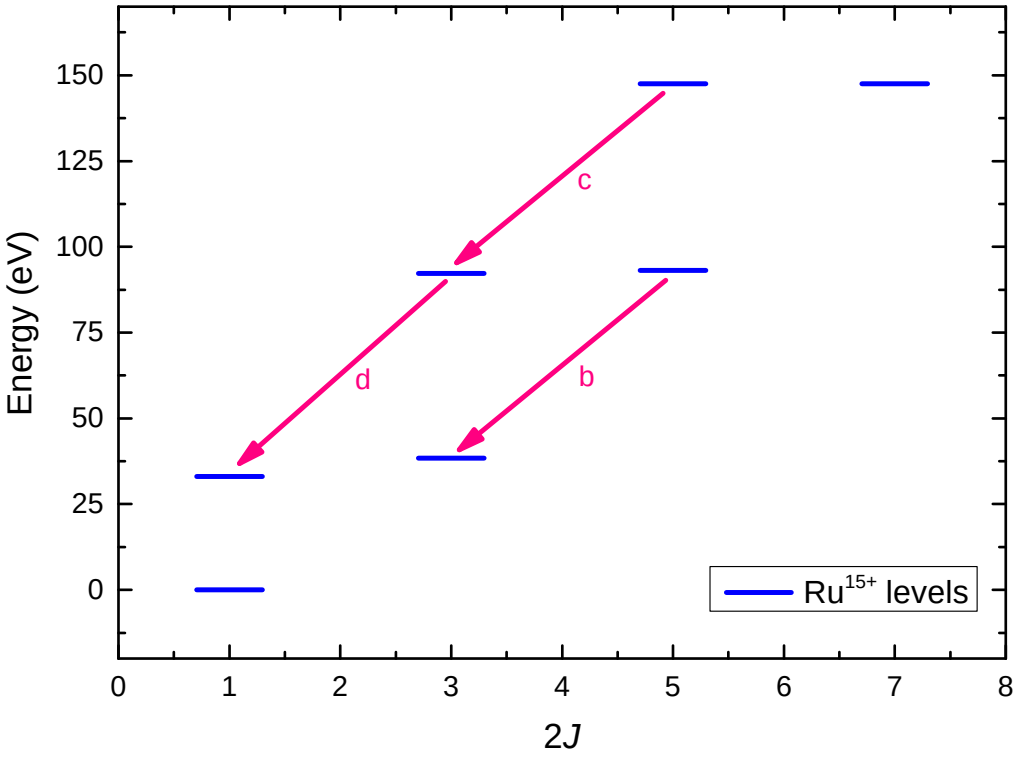

Figure 5.6: Comparison between experimental and theoretical Ru^{15+} spectra. The lines from the experiment and theory are shown in black and red, respectively. Identified transitions are listed from a) to d). The theoretical calculations were obtained with FAC.

Figures 5.5 and 5.6 show the experiment and theory comparison and Grotrian level diagrams for the electronic transitions of Ru^{15+}, respectively. Three transitions are identified and they are listed from b) to d), and their corresponding values are showcased in table 5.4.

We can qualitatively observe from figure 5.5 that the peaks b) and d) have the good agreement with the theory in terms of photon energy, but a noticeable translation to the left can still be easily observed. And it can also be seen that the intensity of line c) does not match up with the theoretical predictions. Again, these discrepancies between the theoretical calculations and the experimental measurement could stem from various sources. But nevertheless, we can confidently state that we have confirmed the state charge identification performed in the previous section, and have identified lines characteristic to the Ru^{14+} and Ru^{15+} ions.

5.2 Two-dimensional theoretical spectra

In order to make a synthetic spectra similar to figure 4.6, we made a complete collisional radiative model using FAC code, following the procedure mentioned in the previous section.

In CRM, we have added all the charge states presented in the experiment, namely from Ru^{8+} and Ru^{16+}. We first calculated their ionization energies. Then we calculated their energy levels, radiative probabilities and cross sections to produce theoretical spectra for each charge state at specific electron beam energies. We produce two dimensional synthetic spectra for the direct comparison with the experimental data (see figure 5.7). It should be noted that this model includes more than two thousand configurations for Ru^{8+} and Ru^{16+} charge states in the calculations. Therefore, it is very time consuming to identify the individual transitions for all the charge states. This is the reason why we have given a 2D representation of both spectra to enable the quick identification of similar features in both spectra. Due to similar reasons, we have limited ourselves to only two charge states which have a few lines for the identification of their respective electronic transitions.

In general, we have found a qualitative agreement between the experiment and the calculations carried out with the FAC code. We have marked a few common features (or transitions) in both spectra with numbers from 1 to 10.

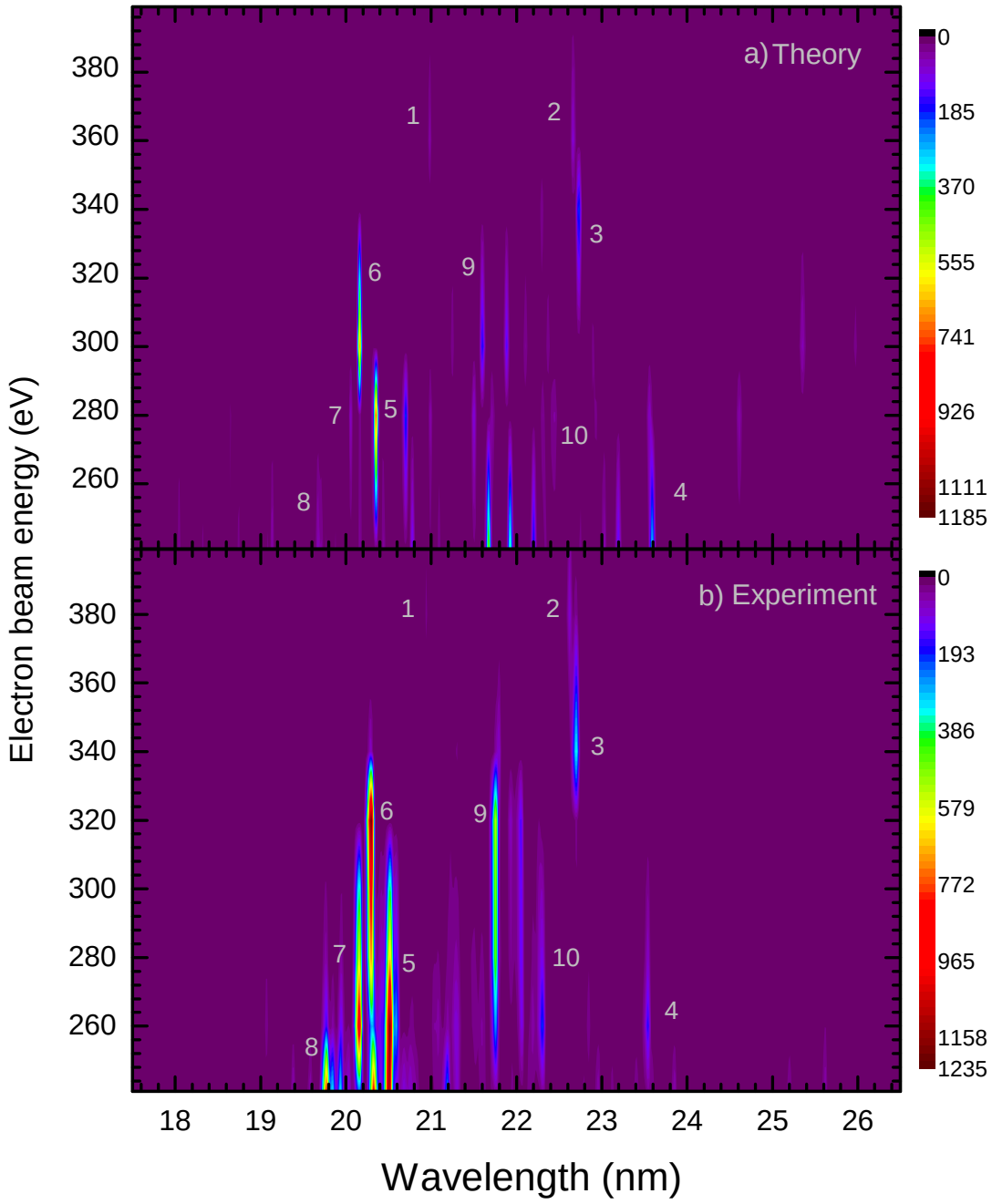

Figure 5.7: Two dimensional representation of the theoretical and experimental Ru-ion spectra. (a) Theoretical spectrum computed using FAC code. The electron beam density is selected to be 10^{10}cm^{-3}. (b) Experiment spectra measured at a fixed beam current of 15 mA.

6 Summary and Outlook

The primary aim of this thesis was to observe and identify lines of ruthenium ions in the ultraviolet regime for charge states with no data currently available. This was for the astrophysical purpose of identifying ruthenium, and eventually technetium in the spectrum of helium-rich white dwarfs. The identification of charge states is also useful to compare with theoretical calculations focusing on many electron systems. Having more atomic data is of paramount importance to test different theoretical predictions.

A total of ten electronic transitions in the EUV wavelength range were identified for the first time: 7 transitions for Ru^{14+} and 3 transitions for Ru^{15+}. They were found in the wavelength range 17 – 26 nm. To achieve this, ruthenium was injected into the FLASH-EBIT, which was operated at an electron beam current of 15 mA, taking measurements at beam energies in the range between 240 and 440 eV at 20 eV intervals. The trap depth was set to $\sim$ 100 V. The spectra were recorded using an EUV spectrometer attached to the EBIT. Small corrections had to be made since the images were slightly shifted to one side (see figure 4.2). In order to calibrate the Ru-ions spectra, we measured well-known iron lines at the same camera height as the ruthenium measurements. Iron lines ranging from Fe^{9+} to Fe^{23+} were identified and a polynomial fit was made to calibrate the CCD camera. The iron spectra were recorded before the ruthenium measurements, so additional steps had to be taken to ensure that no lines from Fe-ions were present in the ruthenium spectra. The charge states were then identified by plotting the evolution of the line intensities as a function of the electron beam energy. The Ru^{14+} and Ru^{15+} spectra were discussed in more detail.

As previously mentioned, both charge states were compared to FAC calculations. Qualitative agreement was found with the theory, but some inconsistencies between the measurements and the theoretical predictions were seen, particularly with the intensity. These discrepancies likely arise from a combination of factors. The effective electron beam energy in the trap could vary for different charge states, which would result in a change from the predicted intensities. It's not uncommon for theoretical models to disagree with each other and with experimental data due to the high complexity of calculations [25]. This is why having more spectral data to compare against these models becomes more important.

In the future, EUV lines from the other presented charge states from the ruthenium ions can be identified with more accurate calculations. The tables and figures for those charge states are provided in the appendix for this very reason. Taking

measurements at lower energies would also be a goal for the future which would allow us to access the lower charge states of ruthenium ions. Similar measurements at an EBIT are planned for highly ionized technetium which is very important to understand the evolutionary history of the white dwarf star RE 0503-289. For this purpose, a vacuum ultraviolet spectrometer (30 – 180 nm) is being developed. An injection system specific for technetium is also planned, since special requirements need to be met due to the radioactive nature of technetium. The long term goal would be to produce experimental and theoretical data for various trans-iron elements (important for astrophysics) to complete the large gaps in the atomic data for highly charged ions (see figure 1.3).

Appendix

As previously mentioned, the number of lines observed in the present experiment is exhaustive and a comprehensive analysis was not feasible. However, we still provide a complete table with observed wavelength values for the future line identification to benchmark different theories and the calculations used in astrophysical models.

The original uncorrected CCD images are seen at the top. Below, the corresponding intesity vs. wavelength graphs are shown in linear and logarithmic scales. The extracted line positions are given in tables 6.1 to 6.9 in pixels as well as in wavelength.

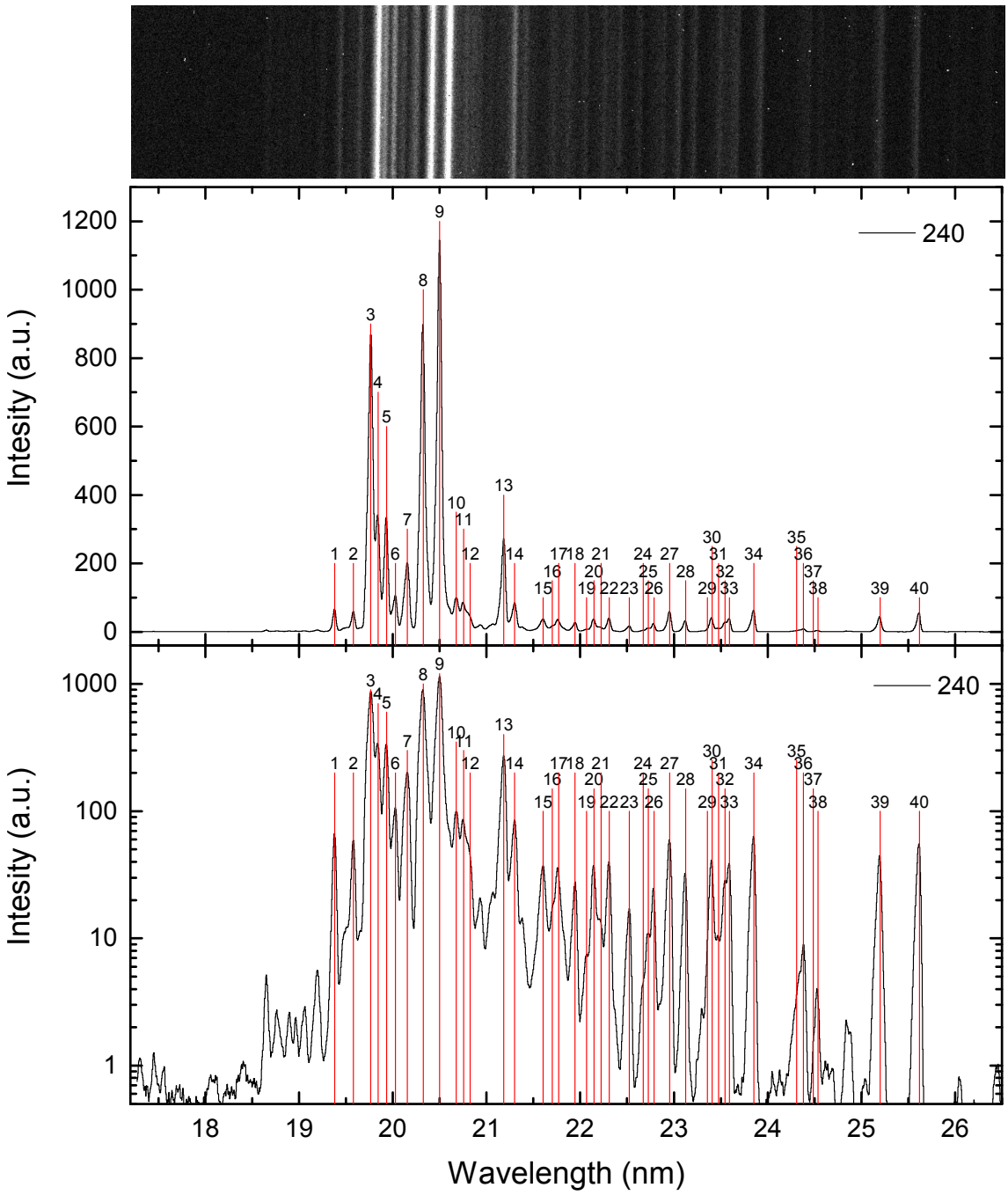

Figure 6.1: Top: uncorrected CCD image obtained at an electron beam energy of 240 eV. Bottom: Ru-ion peaks at E_{beam}=240 eV, in linear and logarithmic scale. Peak centroids are shown with the labelled red lines.

Table 6.1: Peak positions at an electron beam energy of 240 eV. L represents the label number in figure 6.1, Pixel and ΔPixel are the peak positions in pixel and its error , and λ and $\Delta\lambda$ are the wavelength position and its error in nm.

L	Pixel	ΔPixel	λ (nm)	$\Delta\lambda$ (nm)
1	496.402	0.108	19.381	0.003
2	542.154	0.274	19.580	0.004
3	584.447	0.111	19.765	0.004
4	602.008	0.332	19.842	0.004
5	622.647	0.297	19.933	0.004
6	644.585	0.874	20.030	0.005
7	672.619	0.160	20.154	0.004
8	711.035	0.175	20.324	0.004
9	750.864	0.139	20.501	0.005
10	789.853	0.206	20.675	0.005
11	808.152	0.404	20.757	0.005
12	823.374	0.588	20.825	0.006
13	903.342	0.194	21.185	0.006
14	928.613	0.290	21.299	0.006
15	995.769	0.173	21.604	0.006
16	1017.034	0.819	21.701	0.007
17	1032.217	0.270	21.770	0.007
18	1070.709	0.224	21.946	0.007
19	1097.447	0.469	22.069	0.007
20	1114.802	0.110	22.148	0.007
21	1130.627	0.257	22.221	0.007
22	1149.941	0.096	22.310	0.007
23	1195.956	0.196	22.523	0.008
24	1227.918	0.457	22.671	0.008
25	1240.009	0.212	22.728	0.008
26	1252.676	0.083	22.787	0.008
27	1288.952	0.148	22.956	0.008
28	1324.746	0.136	23.123	0.009
29	1374.624	0.704	23.357	0.009
30	1385.223	0.102	23.407	0.009
31	1400.130	0.280	23.478	0.009
32	1414.134	0.159	23.544	0.009
33	1424.715	0.103	23.594	0.009
34	1479.144	0.144	23.851	0.010
35	1574.927	0.668	24.308	0.011
36	1590.612	0.261	24.383	0.011
37	1612.007	1.402	24.486	0.012
38	1622.624	0.236	24.537	0.011
39	1759.707	0.142	25.199	0.012
40	1845.725	0.145	25.619	0.013

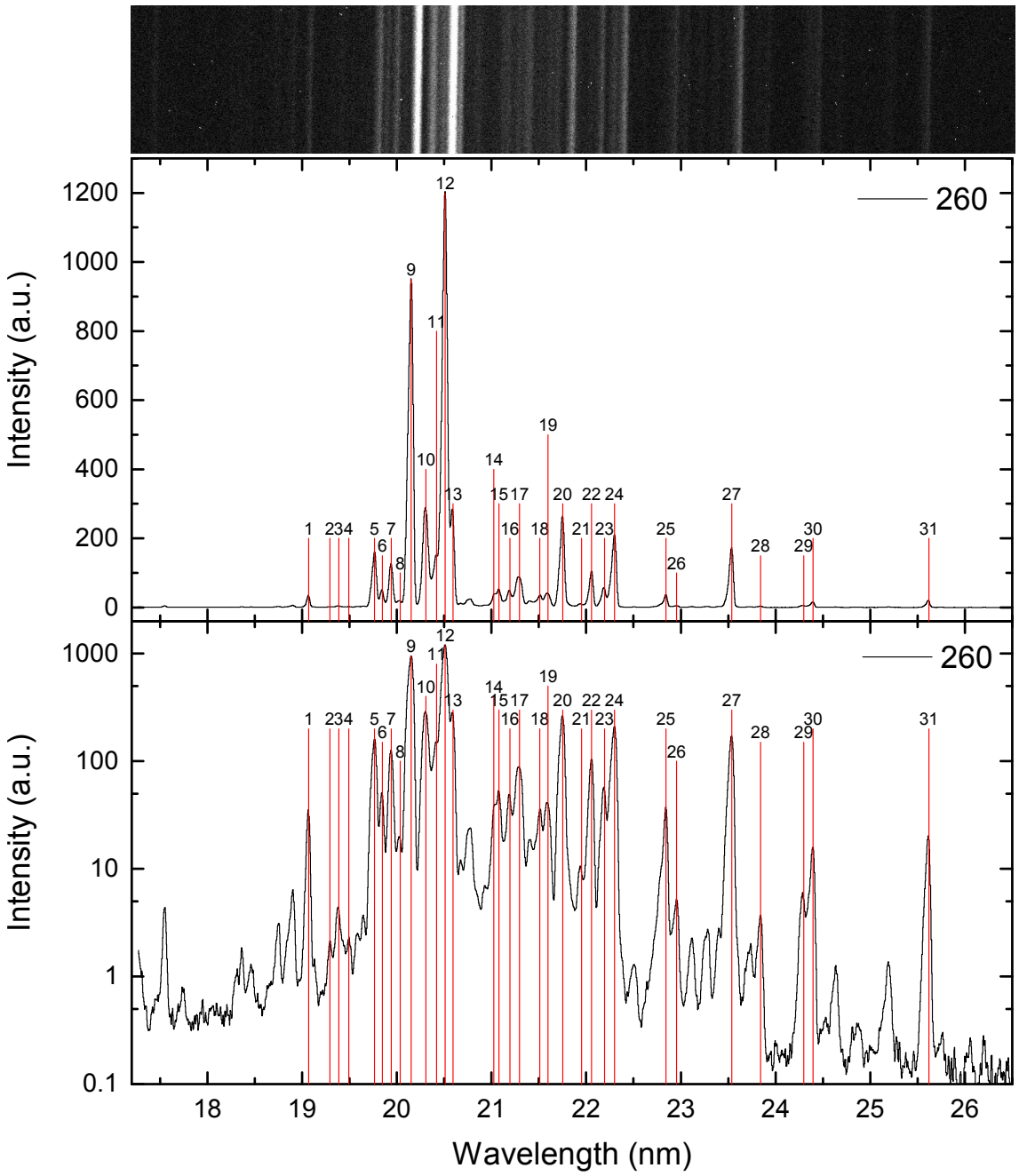

Figure 6.2: Top: uncorrected CCD image obtained at an electron beam energy of 260 eV. Bottom: Ru-ion peaks at E_{beam}=260 eV, in linear and logarithmic scale. Peak centroids are shown with the labelled red lines.

Table 6.2: Peak positions at an electron beam energy of 260 eV. L represents the label number in figure 6.2, Pixel and ΔPixel are the peak positions in pixel and its error, and λ and $\Delta\lambda$ are the wavelength position and its error in nm.

L	Pixel	ΔPixel	λ (nm)	$\Delta\lambda$ (nm)
1	424.091	0.085	19.067	0.003 [t]
2	475.908	0.510	19.292	0.004
3	497.934	0.213	19.387	0.003
4	522.328	0.377	19.494	0.004
5	584.310	0.095	19.765	0.004
6	603.045	0.334	19.847	0.004
7	624.597	0.121	19.942	0.004
8	645.672	0.713	20.035	0.005
9	671.795	0.145	20.150	0.004
10	707.392	0.251	20.308	0.005
11	732.693	0.520	20.420	0.005
12	753.049	0.076	20.511	0.005
13	771.464	0.422	20.593	0.005
14	868.061	1.013	21.026	0.007
15	880.224	0.531	21.080	0.006
16	905.262	0.247	21.193	0.006
17	927.700	0.104	21.295	0.006
18	975.309	0.213	21.511	0.006
19	994.238	0.152	21.597	0.006
20	1028.137	0.123	21.751	0.006
21	1072.127	0.986	21.952	0.008
22	1095.166	0.123	22.058	0.007
23	1124.616	0.499	22.194	0.007
24	1147.513	0.137	22.299	0.007
25	1264.868	0.219	22.843	0.008
26	1288.876	1.349	22.955	0.010
27	1412.963	0.144	23.538	0.009
28	1477.322	0.194	23.843	0.010
29	1572.594	0.486	24.297	0.011
30	1593.215	0.211	24.396	0.011
31	1845.692	0.148	25.619	0.013

Table 6.3: Peak positions at an electron beam energy of 280 eV. L represents the label number in figure 6.3, Pixel and ΔPixel are the peak positions in pixel and its error , and λ and $\Delta\lambda$ are the wavelength position and its error in nm.

L	Pixel	ΔPixel	λ (nm)	$\Delta\lambda$ (nm)
1	66.207	0.837	17.547	0.004
2	349.812	0.898	18.747	0.005
3	385.619	0.515	18.901	0.004
4	424.558	0.103	19.069	0.003
5	583.310	0.086	19.760	0.004
6	603.795	0.442	19.850	0.004
7	625.301	0.108	19.945	0.004
8	671.853	0.149	20.150	0.004
9	703.944	0.116	20.292	0.004
10	733.022	0.677	20.421	0.005
11	753.286	0.088	20.512	0.005
12	771.182	0.515	20.591	0.005
13	910.226	0.192	21.216	0.006
14	928.028	0.138	21.296	0.006
15	953.608	0.336	21.412	0.006
16	972.196	0.161	21.496	0.006
17	994.246	0.132	21.597	0.006
18	1027.891	0.127	21.750	0.006
19	1068.929	0.451	21.938	0.007
20	1093.581	0.147	22.051	0.007
21	1126.073	0.693	22.200	0.008
22	1145.992	0.154	22.292	0.007
23	1185.091	0.234	22.473	0.008
24	1234.060	0.285	22.700	0.008
25	1265.628	0.285	22.847	0.008
26	1413.135	0.121	23.539	0.009
27	1592.875	0.517	24.394	0.011
28	1845.735	0.194	25.619	0.013
29	1873.274	0.188	25.754	0.013

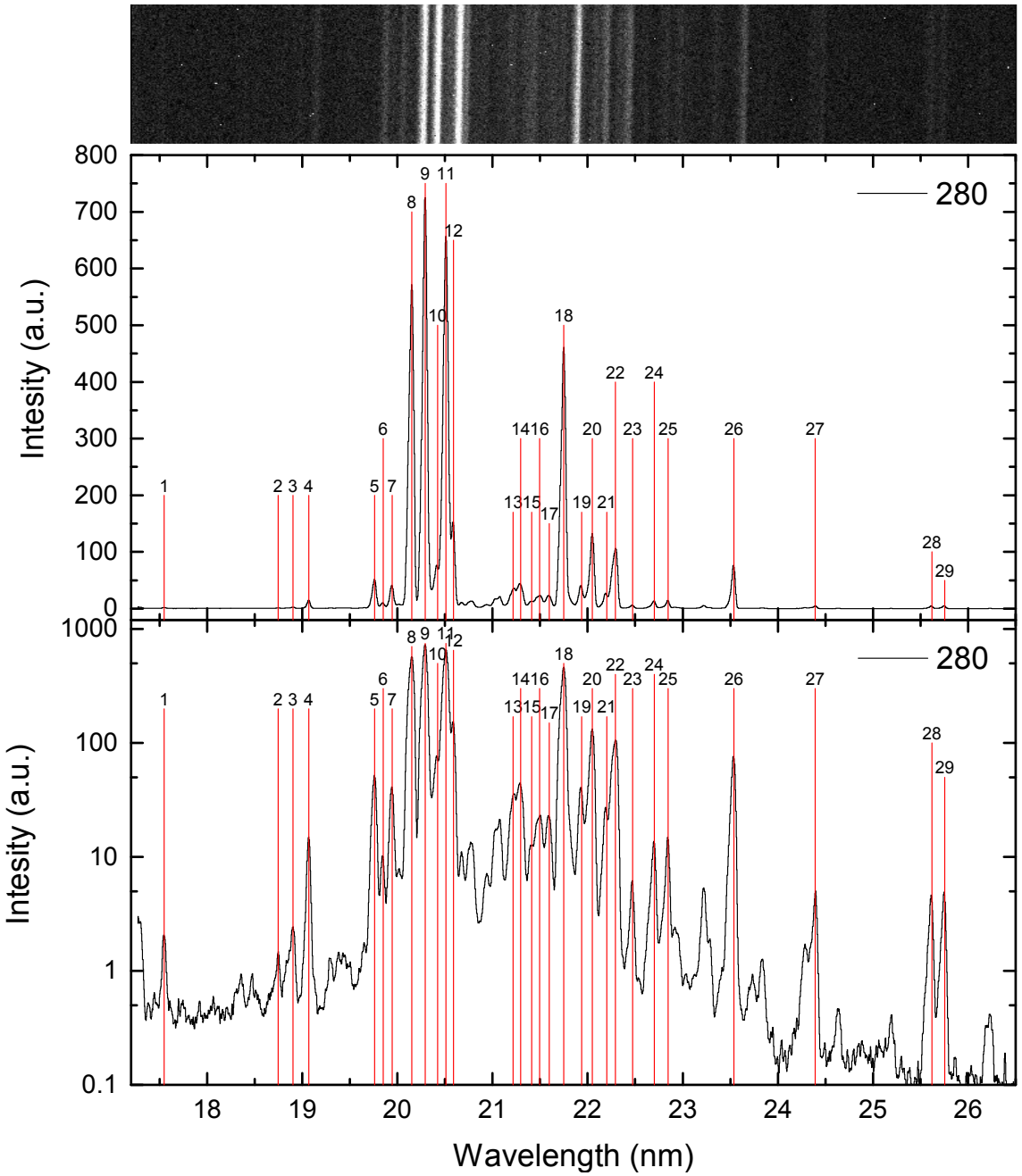

Figure 6.3: Top: uncorrected CCD image obtained at an electron beam energy of 280 eV. Bottom: Ru-ion peaks at E_{beam}=280 eV, in linear and logarithmic scale. Peak centroids are shown with the labelled red lines.

Table 6.4: Peak positions at an electron beam energy of 300 eV. L represents the label number in figure 6.4, Pixel and ΔPixel are the peak positions in pixel and its error , and λ and $\Delta\lambda$ are the wavelength position and its error in nm.

L	Pixel	ΔPixel	λ (nm)	$\Delta\lambda$ (nm)
1	424.776	0.113	19.070	0.003
2	583.035	0.095	19.759	0.004
3	604.147	0.465	19.852	0.004
4	625.713	0.114	19.947	0.004
5	672.018	0.253	20.151	0.004
6	703.569	0.104	20.291	0.004
7	732.958	0.725	20.421	0.005
8	753.598	0.083	20.513	0.005
9	771.433	0.552	20.593	0.005
10	790.757	0.323	20.679	0.005
11	813.569	0.250	20.781	0.005
12	848.299	0.418	20.937	0.006
13	869.073	0.780	21.030	0.006
14	881.237	0.559	21.085	0.006
15	911.519	0.212	21.222	0.006
16	928.432	0.212	21.298	0.006
17	952.704	0.266	21.408	0.006
18	971.797	0.123	21.495	0.006
19	994.149	0.122	21.596	0.006
20	1027.895	0.133	21.750	0.006
21	1068.574	0.409	21.936	0.007
22	1093.136	0.153	22.049	0.007
23	1126.098	0.723	22.200	0.008
24	1145.090	0.150	22.288	0.007
25	1184.593	0.244	22.470	0.008
26	1233.956	0.225	22.699	0.008
27	1265.844	0.237	22.848	0.008
28	1346.217	0.212	23.224	0.009
29	1413.195	0.163	23.539	0.009
30	1571.147	0.483	24.290	0.011
31	1593.082	0.260	24.395	0.011
32	1845.579	0.239	25.618	0.013
33	1873.580	0.180	25.755	0.013

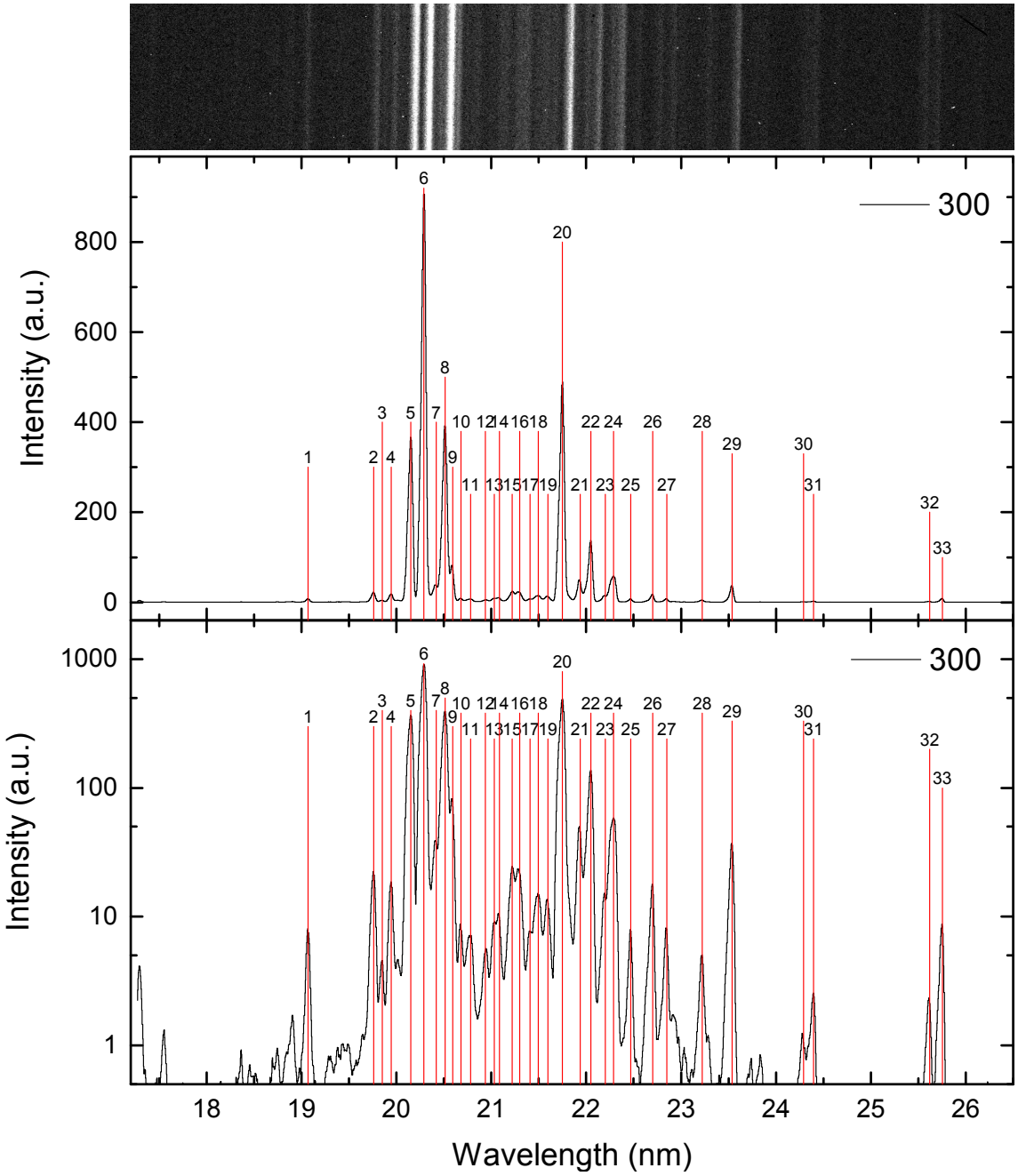

Figure 6.4: Top: uncorrected CCD image obtained at an electron beam energy of 300 eV. Bottom: Ru-ion peaks at E_{beam}=300 eV, in linear and logarithmic scale. Peak centroids are shown with the labelled red lines.

Table 6.5: Peak positions at an electron beam energy of 320 eV. L represents the label number in figure 6.5, Pixel and ΔPixel are the peak positions in pixel and its error , and λ and $\Delta\lambda$ are the wavelength position and its error in nm.

L	Pixel	ΔPixel	λ (nm)	$\Delta\lambda$ (nm)
1	427.317	0.399	19.081	0.003
2	580.996	0.226	19.750	0.004
3	703.431	0.159	20.290	0.004
4	791.196	0.245	20.681	0.005
5	849.284	0.221	20.941	0.005
6	912.043	0.155	21.224	0.006
7	951.156	0.381	21.401	0.006
8	970.251	0.119	21.488	0.006
9	994.594	0.275	21.598	0.006
10	1027.902	0.131	21.750	0.006
11	1068.312	0.310	21.935	0.007
12	1092.391	0.160	22.045	0.007
13	1139.272	0.136	22.261	0.007
14	1184.718	0.160	22.471	0.008
15	1233.778	0.216	22.699	0.008
16	1345.046	0.145	23.218	0.009
17	1873.561	0.125	25.755	0.013

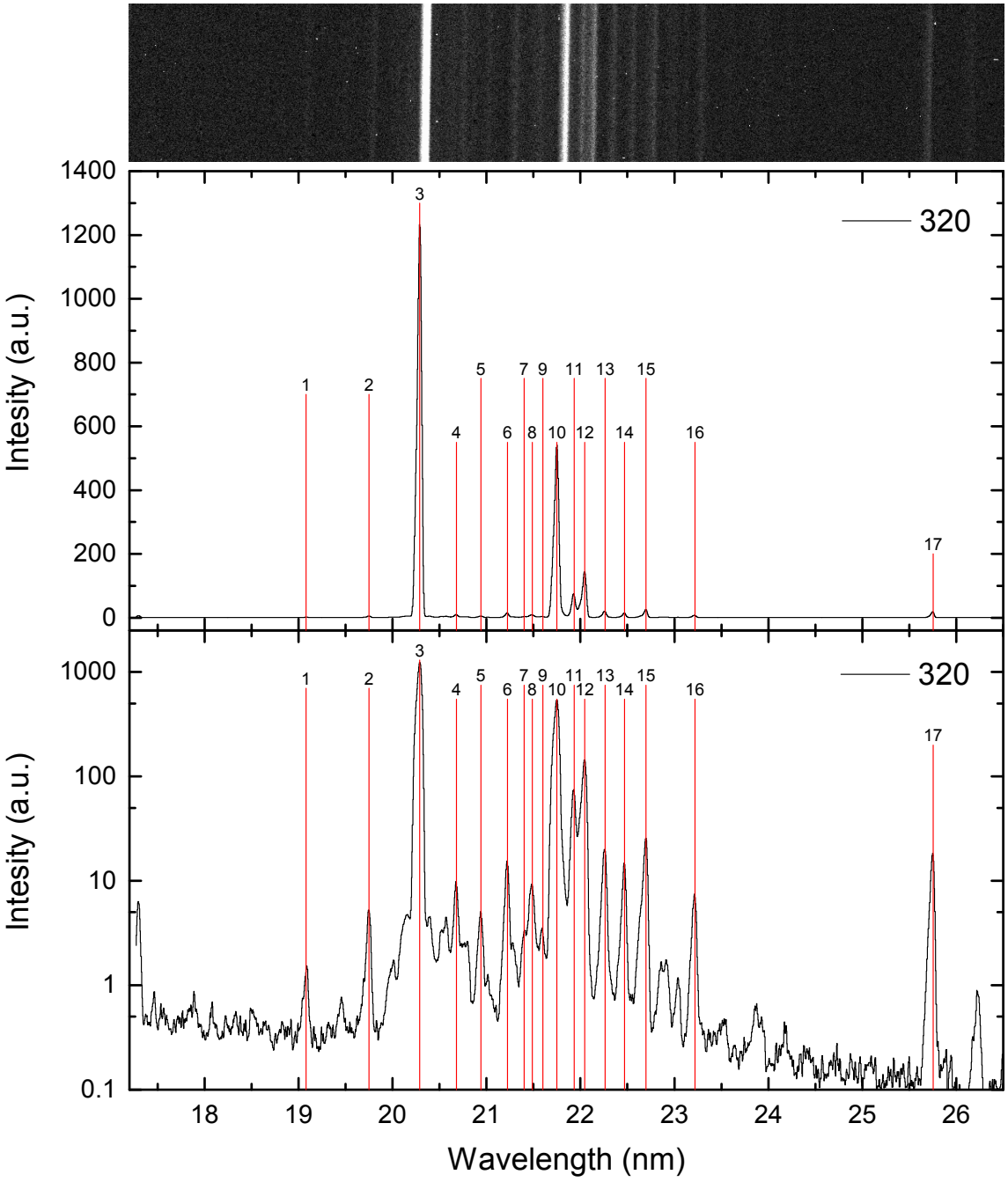

Figure 6.5: Top: uncorrected CCD image obtained at an electron beam energy of 320 eV. Bottom: Ru-ion peaks at E_{beam}=320 eV, in linear and logarithmic scale. Peak centroids are shown with the labelled red lines.

Table 6.6: Peak positions at an electron beam energy of 360 eV. L represents the label number in figure 6.6, Pixel and ΔPixel are the peak positions in pixel and its error , and λ and $\Delta\lambda$ are the wavelength position and its error in nm.

L	Pixel	ΔPixel	λ (nm)	$\Delta\lambda$ (nm)
1	295.761	0.298	18.516	0.003
2	537.742	0.290	19.561	0.004
3	701.740	0.090	20.283	0.004
4	768.134	0.091	20.578	0.005
5	793.485	0.478	20.691	0.005
6	810.170	1.100	20.766	0.007
7	849.196	0.092	20.941	0.005
8	929.299	0.076	21.302	0.006
9	1037.600	0.104	21.794	0.006
10	1147.696	0.227	22.300	0.007
11	1220.766	0.296	22.638	0.008
12	1234.105	0.075	22.700	0.008

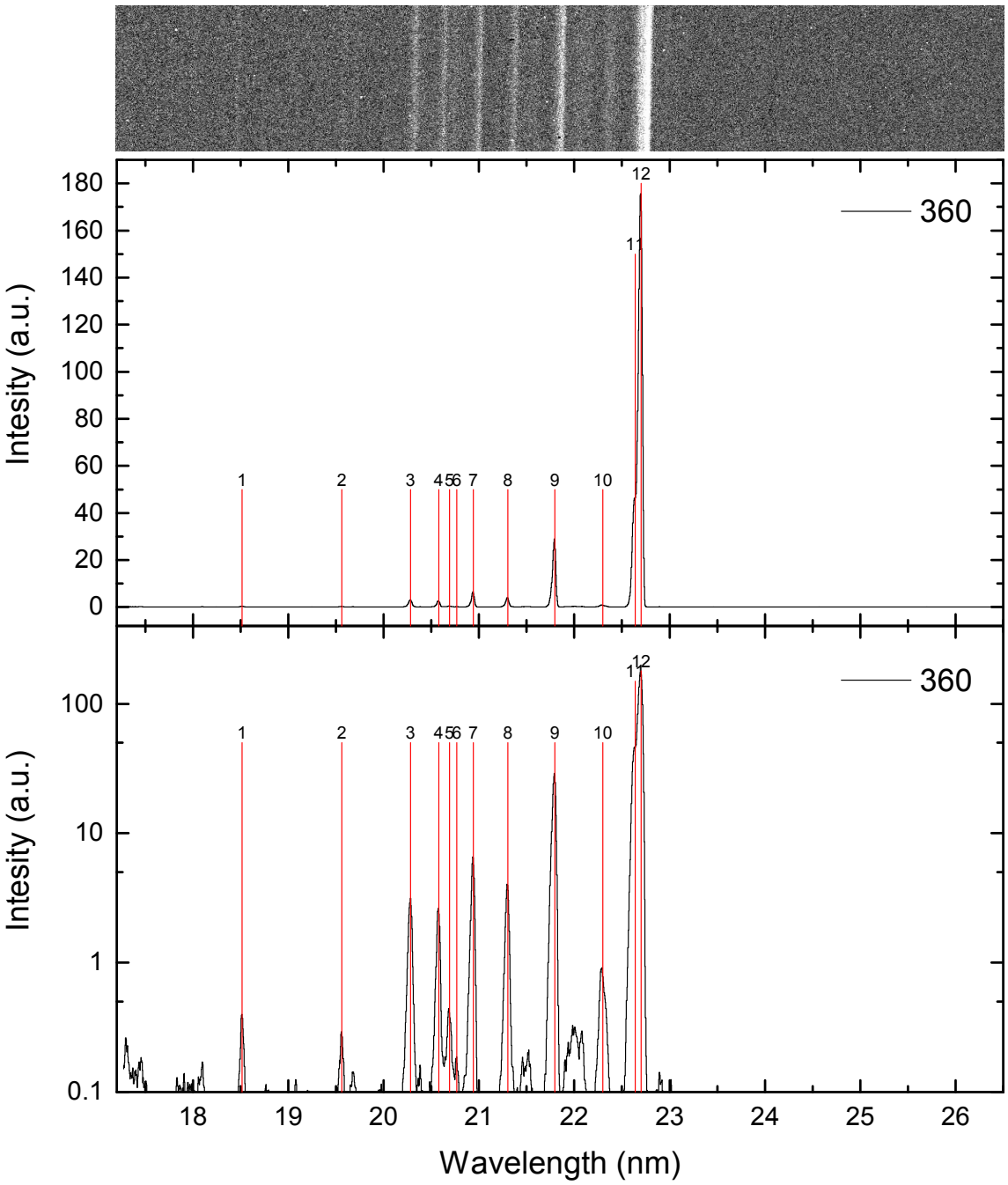

Figure 6.6: Top: uncorrected CCD image obtained at an electron beam energy of 360 eV. Bottom: Ru-ion peaks at E_{beam}=360 eV, in linear and logarithmic scale. Peak centroids are shown with the labelled red lines.

Table 6.7: Peak positions at an electron beam energy of 400 eV. L represents the label number in figure 6.7, Pixel and ΔPixel are the peak positions in pixel and its error , and λ and $\Delta\lambda$ are the wavelength position and its error in nm.

L	Pixel	ΔPixel	λ (nm)	$\Delta\lambda$ (nm)
1	538.872	0.200	19.566	0.004
2	849.888	0.038	20.944	0.005
3	1146.947	0.388	22.297	0.007
4	1217.773	0.049	22.624	0.008
5	1233.653	1.056	22.698	0.009

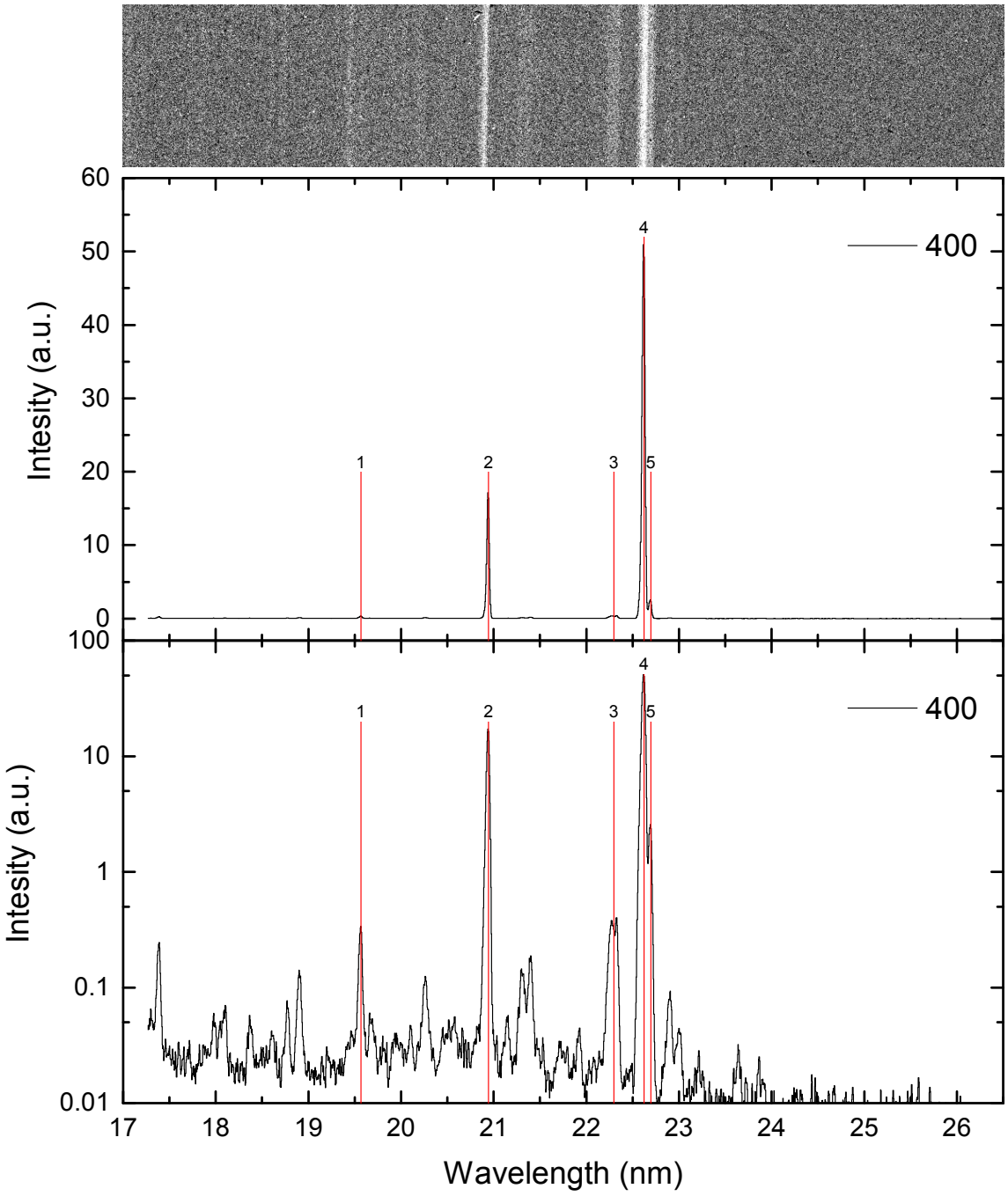

Figure 6.7: Top: uncorrected CCD image obtained at an electron beam energy of 400 eV. Bottom: Ru-ion peaks at E_{beam}=400 eV, in linear and logarithmic scale. Peak centroids are shown with the labelled red lines.

Table 6.8: Peak positions at an electron beam energy of 420 eV. L represents the label number in figure 6.8, Pixel and ΔPixel are the peak positions in pixel and its error , and λ and $\Delta\lambda$ are the wavelength position and its error in nm.

L	Pixel	ΔPixel	λ (nm)	$\Delta\lambda$ (nm)
1	26.284	0.285	17.380	0.002
2	316.759	0.396	18.606	0.003
3	355.726	0.546	18.773	0.004
4	387.248	0.148	18.908	0.003
5	538.497	0.322	19.564	0.004
6	697.965	0.426	20.266	0.005
7	849.779	0.075	20.943	0.005
8	930.873	0.311	21.309	0.006
9	952.148	0.380	21.405	0.006
10	1141.774	0.248	22.273	0.007
11	1153.756	0.619	22.328	0.008
12	1217.623	0.060	22.624	0.008
13	1233.398	1.056	22.697	0.009

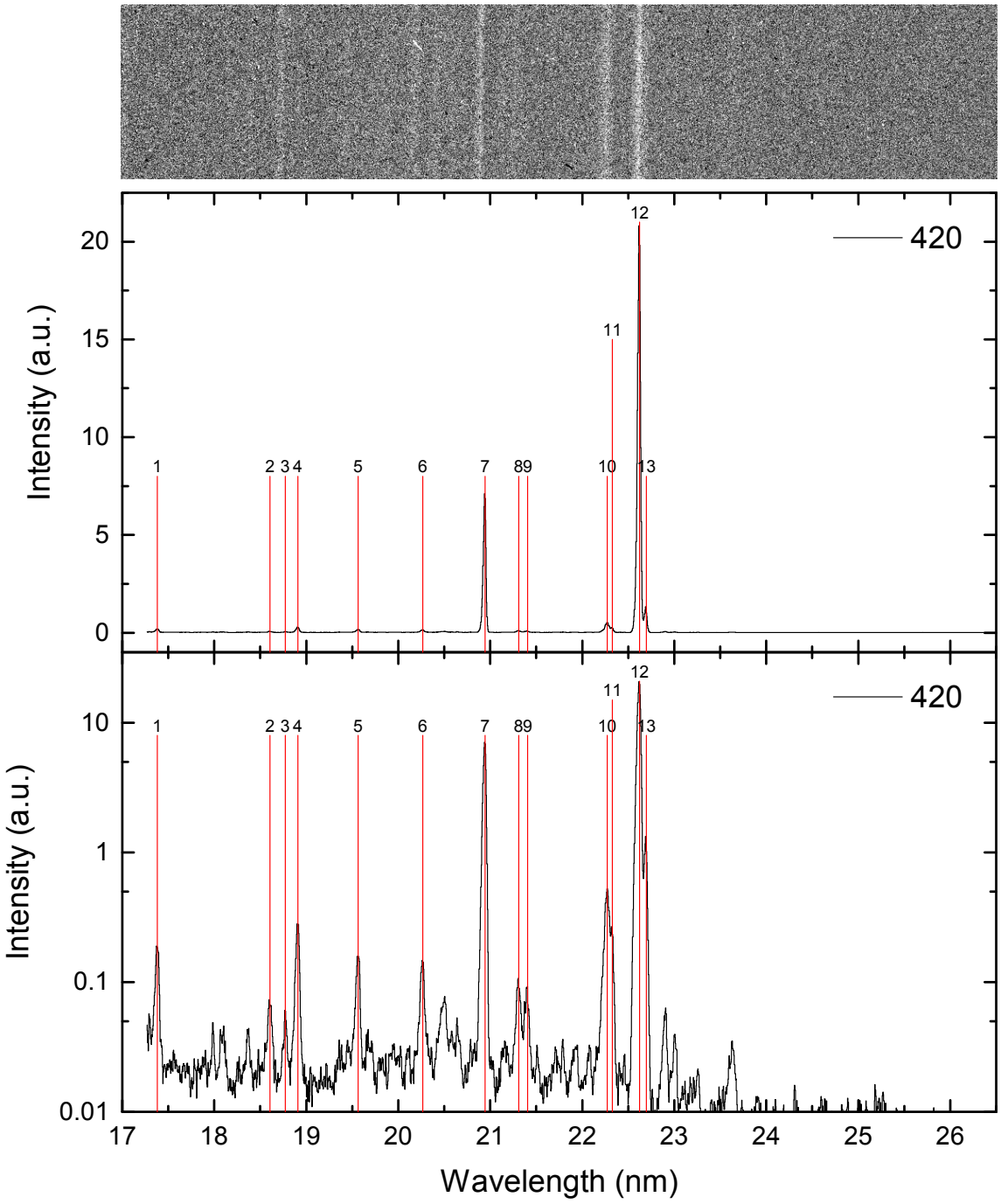

Figure 6.8: Top: uncorrected CCD image obtained at an electron beam energy of 420 eV. Bottom: Ru-ion peaks at E_{beam}=420 eV, in linear and logarithmic scale. Peak centroids are shown with the labelled red lines.

Table 6.9: Peak positions at an electron beam energy of 440 eV. L represents the label number in figure 6.9, Pixel and ΔPixel are the peak positions in pixel and its error , and λ and $\Delta\lambda$ are the wavelength position and its error in nm.

L	Pixel	ΔPixel	λ (nm)	$\Delta\lambda$ (nm)
1	24.816	0.369	17.374	0.002
2	70.523	0.409	17.565	0.003
3	317.256	0.449	18.608	0.003
4	387.438	0.095	18.909	0.003
5	697.681	0.368	20.265	0.005
6	747.825	0.364	20.487	0.005
7	849.256	0.100	20.941	0.005
8	1140.926	0.172	22.269	0.007
9	1217.741	0.047	22.624	0.008
10	1233.310	1.168	22.696	0.009

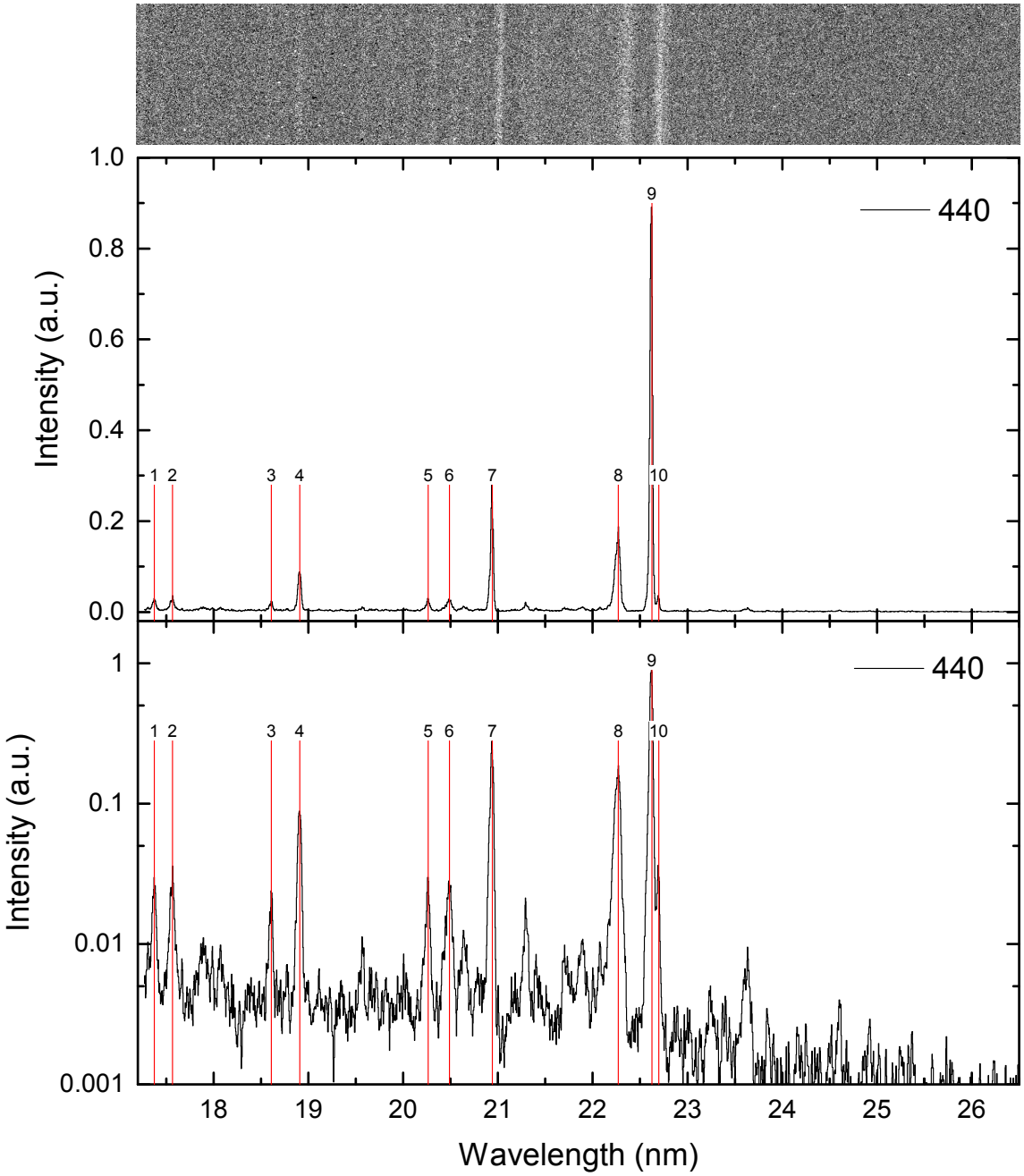

Figure 6.9: Top: uncorrected CCD image obtained at an electron beam energy of 440 eV. Bottom: Ru-ion peaks at E_{beam}=440 eV, in linear and logarithmic scale. Peak centroids are shown with the labelled red lines.

Bibliography

[1] G. Kirchhoff and R. Bunsen, "Chemische analyse durch spectralbeobachtungen," *Annalen der Physik* **186** no. 6, (1860) 161–189.

[2] H. P. Warren, "Measurements of absolute abundances in solar flares," *The Astrophysical Journal Letters* **786** no. 1, (2014) L2.

[3] S. K. Solanki and E. Marsch, *Solar Space Missions: present and future*, pp. 229–248. Wiley-VCH Verlag GmbH & Co. KGaA, 2010.

[4] K. Werner, T. Rauch, E. Ringat, and J. W. Kruk, "First Detection of Krypton and Xenon in a White Dwarf," *The Astrophysical Journal* **753** (2012) L7.

[5] M. A. Barstow, J. B. Holberg, T. A. Fleming, M. C. Marsh, D. Koester, and D. Wonnacott, "A ROSAT Survey of Hot DA White Dwarfs in Non-Interacting Binary Systems," *MNRAS* **270** (1994) 499.

[6] S. Dreizler and K. Werner, "Spectral analysis of hot helium-rich white dwarfs.," *A&A* **314** (1996) 217–232.

[7] Werner, K., Rauch, T., Kučas, S., and Kruk, J. W., "The prospective search for highly ionized technetium in hot (pre-) white dwarfs," *A&A* **574** (2015) A29.

[8] K. Werner and J. R. Crespo, "Search for technetium in extremely hot evolved stars.".

[9] H. Chen, P. Beiersdorfer, L. A. Heeter, D. A. Liedahl, K. L. Naranjo-Rivera, E. Träbert, M. F. Gu, and J. K. Lepson, "Experimental and Theoretical Evaluation of Density-sensitive N VI, Ar XIV, and Fe XXII Line Ratios," *The Astrophysical Journal* **611** no. 1, (2004) 598. http://stacks.iop.org/0004-637X/611/i=1/a=598.

[10] N. Yamamoto, T. Kato, H. Funaba, K. Sato, N. Tamura, S. Sudo, P. Beiersdorfer, and J. K. Lepson, "Measurement and modeling of density-sensitive lines of fe xiii in the extreme ultraviolet," *The Astrophysical Journal* **689** no. 1, (2008) 646.

[11] B. Bransden and C. Joachain, *Physics of Atoms and Molecules*. Pearson Education. Prentice Hall, 2003.

[12] S. Jochim, "Experimentalphysik IV SS 2014.".

[13] J. Gillaspy, *Trapping Highly Charged Ions: Fundamentals and Applications*. Nova Science Publishers, 2001.

[14] S. Dobrodey, "KLL-dielectronic recombination resonances and simultaneous VUV transitions in highly charged iron," 2014.

[15] H. Jeanperrin, "Extreme ultraviolet spectroscopy of highly charged W ions relevant to fusion plasmas: The W XIV-W XVI transitions," 2014.

[16] C. Shah, *Measuring and modeling of anisotropic and polarized X-ray emission following resonant recombination into highly charged ions*. PhD thesis, Ruprecht-Karls-Universität Heidelberg, 2015.

[17] S. Bernitt, *Resonant excitation of astrophysical X-ray transitions in highly charged iron ions with the free-electron laser LCLS*. PhD thesis, Ruprecht-Karls-Universität Heidelberg, 2013.

[18] L. Brillouin, "A theorem of larmor and its importance for electrons in magnetic fields," *Phys. Rev.* **67** (Apr, 1945) 260–266.

[19] G. Herrmann, "Optical theory of thermal velocity effects in cylindrical electron beams," *Journal of Applied Physics* **29** no. 2, (1958) 127–136.

[20] G. Y. Liang, "Extreme-ultraviolet spectroscopy of Fe VI – Fe XV and its diagnostic application for electron beam ion trap plasmas," *The Astrophysical Journal* **696** (2009) 2275.

[21] F. Currell, "Physics of and with Electron Beam Ion Traps and Sources EBIS/T.".

[22] R. Soria Orts, *Isotopic effect in B-like and Be-like argon ions*. PhD thesis, Johann Wolfgang Göthe - Universität, 2005.

[23] T. Baumann, "Development of a grating spectrometer for vacuum ultraviolet radiation from highly charged ions," 2008.

[24] J. Samson and D. Ederer, *Vacuum Ultraviolet Spectroscopy*. Experimental methods in the physical sciences. Elsevier Science, 2000.

[25] H. Bekker, *Optical and EUV spectroscopy of highly charged ions near the 4 f–5s level crossing*. PhD thesis, Ruprecht-Karls-Universität Heidelberg, 2016.

[26] G. Y. Liang, J. R. C. López-Urrutia, T. M. Baumann, S. W. Epp, A. Gonchar, A. Lapierre, P. H. Mokler, M. C. Simon, H. Tawara, V. Mäckel, K. Yao, G. Zhao, Y. Zou, and J. Ullrich, "Experimental investigations of ion charge distributions, effective electron densities, and electron-ion cloud overlap in electron beam ion trap plasma using extreme-ultraviolet spectroscopy," *The Astrophysical Journal* **702** no. 2, 838.

[27] "National Institute of Standards and Technology." http://physics.nist.gov/PhysRefData/ASD/lines_form.html.

[28] M. F. Gu, "The flexible atomic code," *Canadian Journal of Physics* **86** no. 5, (2008) 675–689. http://www.nrcresearchpress.com/doi/abs/10.1139/p07-197.

[29] Scofield ,J., "Ionization Energies," *LLNL Internal Report* (1975) .

[30] U. I. Safronova, A. S. Safronova, and P. Beiersdorfer, "Contribution of the $4f$-core-excited states in determination of atomic properties in the promethium isoelectronic sequence," *Phys. Rev. A* **88** (Sep, 2013) 032512.

Acknowledgements

I will add this later ;)

Erklärung

Ich versichere, dass ich diese Arbeit selbstständig verfasst habe und keine anderen als die angegebenen Quellen und Hilfsmittel benutzt habe.

Heidelberg, den 27. März 2017 .....